Heavy Flavor Azimuthal Correlations in PYTHIA Generated Proton-Proton Collisions at LHC Energies

Marius Ole Johansen
Institutt for Fysikk og Teknologi
Universitetet i Bergen
2014

UNIVERSITETET I BERGEN

Abstract

The ALICE detector at CERN is a promising tool for the study of the Quark-Gluon Plasma (QGP), an exotic state of matter thought to be present in the early Universe. The study of partonic energy loss reveals vital information about the interaction between quarks and gluons in the QGP. Heavy quarks are used as probes since they are created in initial hard scattering processes and consequently undergo the entire evolution of the created medium.

Recent studies of hadrons originating from fast light quarks show a suppressed particle yield in events where the QGP is present. For light quarks, the preeminent energy loss is due to radiative energy loss. Heavier quarks are not as sensitive as light quarks to this suppression, but experiments indicates a particle suppression originating from heavy quarks to the same yield as light quarks, implying radiative energy loss is not the only contributor to the partonic energy loss. A study of this energy loss can be performed by utilizing angular correlations of heavy flavor mesons. Alongside yielding important input on energy loss models, the angular correlations also provide a base-line for Pb-Pb collisions and crucial pQCD tests.

In this thesis, the azimuthal correlations of electrons originating from heavy-flavored hadrons and neutral D mesons of PYTHIA simulated proton-proton collisions at several momentum cuts are analyzed. In particular, a new method of obtaining the azimuthal correlations is presented with the aim of both increasing the number of statistics as well as check if there are any significant changes compared to the distributions obtained through the current means. Azimuthal correlations of charm and beauty quarks at different momentum cuts are also analyzed. Due to the low statistics regarding the production of heavy quarks, the analysis will be performed on both a minimum bias run as well as an enhanced sample.

In the 1st chapter, a brief introduction on quarks and matter will be presented alongside some important properties regarding Quark Gluon Plasma. The following chapter will emphasize on the experimental setup at CERN and an outlay of the ALICE detector. Chapter 3 will cover the some important topics regarding the object oriented software AliRoot as well as some fundamental event generators and the main ingredients of an AliAnalysisTask, which is the actual analysis macro. Various heavy flavor production mechanisms and the corresponding Feynman topologies are discussed in Chapter 4. In the succeeding chapter, PYTHIA will be presented with an emphasis on particle production and some examples of generated distributions. Chapter 6 contains the main

analysis of this thesis, namely heavy flavor azimuthal correlations. The various steps of the analysis macro will be introduced, as well as the results from this analysis. A conclusion is given in the final chapter.

Acknowledgements

Finally I am at the end of the long and tedious journey which eventually culminated into my thesis. I would really like to thank everyone who helped me finish this work.

A big thanks to Sedat Altinpinar who made it possible for me to complete this master's thesis. His knowledge and insight into the field of physics has been an inspiration, and he would always come up with solutions to the problems I encountered. I would also like to thank Prof. Dieter Röhrich who introduced me to the field of nuclear physics and I am deeply grateful for all the support he has given me.

I would also like to thank the computer goddess Hege Erdal who taught me the elusive language of GRID and made it possible for me to initiate my analysis in the first place. My fellow students at the office also deserve my gratitude for keeping the collective spirit up in times of need as well as supplementing my knowledge base with all sorts of trivia. Who knows where I would have been today had I remained unaware of the buoyancy of the average fruit fly.

Last I would like to thank all my friends for all the support they have given me!

Contents

List of Figures

List of Tables

x

Chapter 1

Introduction

1.1 A Brief History of Matter

The first scientifically concept of matter has its roots in the ancient Greek natural philosophy known as atomism. Around the 5th century BC, natural philosophers were split into two sides regarding the lore of reality; Heraclitus of Ephesus, who believed that change was the fundamental constituent of all of reality, opposing Parmenides of Elea, instead claiming that change is merely an illusion [1]. Parmenides refused the concept of change and motion, denying the sensorial illusions and instead claiming that reason was the only path to comprehending the apex of the natural sciences.

Democritus was the first natural philosopher to propose the theory of atoms in order to reconcile the two views of nature; all matter is composed of something fundamentally undividable, thus one could have a change of motion, size and position, but not on the cost of the never-changing atoms. The philosophical nature of the atoms changed considerably over time, but the basic concept stood the test of time because of its remarkable elegancy when explaining chemistry. The Greek word for undividable, atomos, is still used today although the atoms have been found to contain smaller constituents.

In 1897, Sir Joseph John Thompson forced a paradigm shift upon the natural sciences when he discovered the electron during one of his cathode ray experiments, consequently annihilating the undividable atom theory [2]. Thompson instead proposed a model where the negatively charged electrons were distributed inside the atom with positive charges to balance out the total charge, a model better known as the plum pudding model. 12 years later, Ernest Rutherford, later known as the father of nuclear physics, conducted an experiment at the University of Manchester where his initiates Hans Geiger and Ernest Marsden bombarded a thin sheet of gold foil in a vacuum chamber with alpha particles generated by a radon source, using a zinc sulfide screen at the base of a microscope as a detector. According to Thompson's model, the incoming alpha particles should experience zero to a few degrees deflection. Although most of the particles behaved according to the pudding model, surprise was imminent when a few number of the deflected particles were scattered at angles even above 90 degrees, completely disobeying the predictions of the prevailing model. The results of the experiment implied that the plum pudding model was incorrect. Instead, Rutherford draw the conclusion that the atom consisted of a positively charged, concentrated mass center, forcing the alpha particles to deflect whenever they directly hit the center or were close
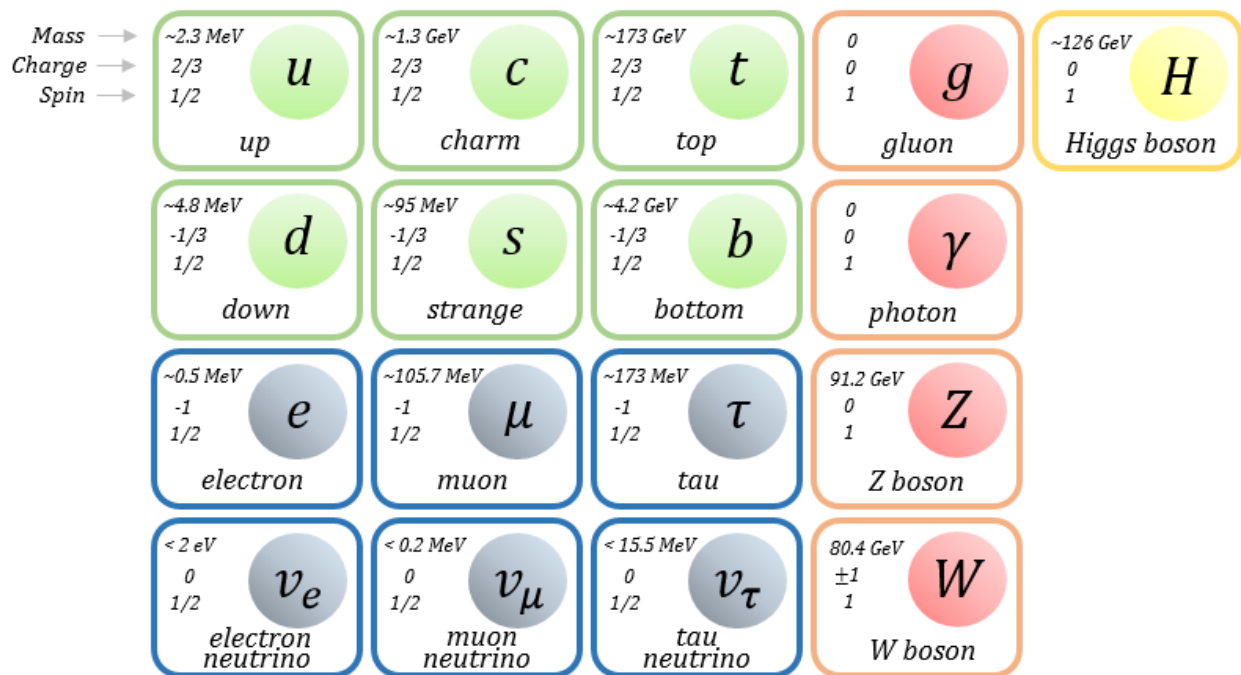
Figure 1.1: The Standard Model of particle physics. Due to the QCD confinement principle, only an approximate measurement of the light quark masses are given.

enough to get deflected. The fact that the majority of the alpha particles traversed the atoms with no deflection implied that the center had to be very small compared to the extent of the atom itself, meaning that the majority of the atom was empty space. In 1911, Rutherford rejected the plum pudding model in a paper and proposed a new model of the atom, where the charge and mass of the atom was mainly concentrated at the center, surrounded by mostly empty space. Two years later, famous physicist Niels Bohr improved Rutherford's model by explaining the distributions of electrons, soon to be replaced by quantum mechanics and the Schrödinger equation which successfully were able to describe and explain the structure of the Hydrogen atom. With the birth of quantum field theory in the 1950s and the discovery of the quarks in the following decade, the Standard Model finally arose, depicting the fundamental particles and how they interact.

According to the Standard Model (see *Figure 1.1*), all matter consists of leptons, quarks and gauge bosons mediating the respectable interactions [3]. Photons and the massive $W^{\pm}$- and Z-bosons are responsible for propagating the electroweak interaction whilst the massless gluons propagate the strong interaction. The field theory describing photon interactions is known as Quantum Electro Dynamics (QED), whilst Quantum Chromo Dynamics (QCD) depicts the strong field regarding the quarks. The Higgs mechanism, utilizing the infamous Higgs boson, is the process responsible for spontaneously symmetry breaking which in return forces mass upon fermions.
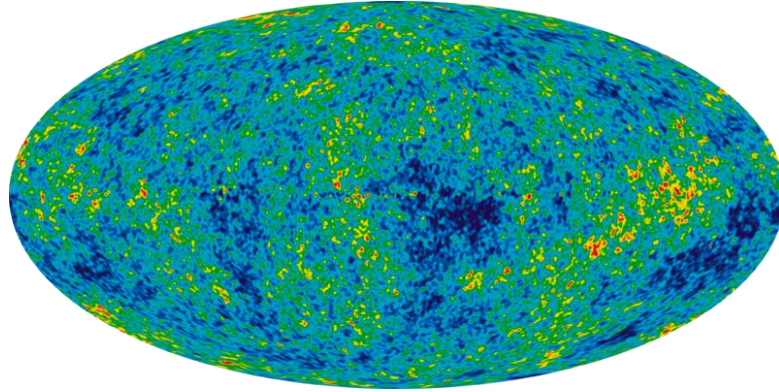
Figure 1.2: Picture of the cosmic microwave background derived from nine years of data from Wilkinson Microwave Anisotropy Probe (WMAP). The color differences represents temperature variations of the left-over radiation from The Big Bang with an average of 2,726 K [4].

1.2 Quark Gluon Plasma

When looking for remnants from the creation of the Universe, few observables can match the cosmic microwave background (CMB). The CMB (see *Figure 1.2*) is a snapshot of left-over radiation from an early stage of the Universe, long before planets, stars and constellations were to be found in the empty void of space and time, dating to roughly 380.000 years after the Big Bang [5]. Although the observable studies of the old Universe stops here, experimentally one is able to recreate conditions even further back in time by using high-energy particle colliders. Before the first hadrons emerged, a soup of free gluons and quarks existed before confining each other in bags of particles. This particle soup is better known as Quark-Gluon Plasma (QGP), an exotic and intriguing phase of matter where quarks are free from the strong interaction. By using super colliders, such as the Large Hadron Collider (LHC) located in Geneva, QGP matter can be recreated by smashing nuclei together at high energies due to the asymptotic freedom of quarks.

Once the confined quarks are "free" from the strong interaction, the QGP can be studied by introducing the nuclear modification factor $R_{AA}(p_T)$, given by

$$R_{AA}(p_T) = \frac{d^2 N_{ch}^{AA} dp_T d\eta}{\langle T_{AA} \rangle d^2 \sigma_{ch}^{NN} dp_T d\eta},$$ (1.1)

where N_{ch}^{AA} is the particle yield in the nucleus-nucleus (AA) collision, σ_{ch}^{NN} is the nucleon-nucleon (NN) collision cross section and $\langle T_{AA} \rangle$ is the nuclear overlap function which is the

3
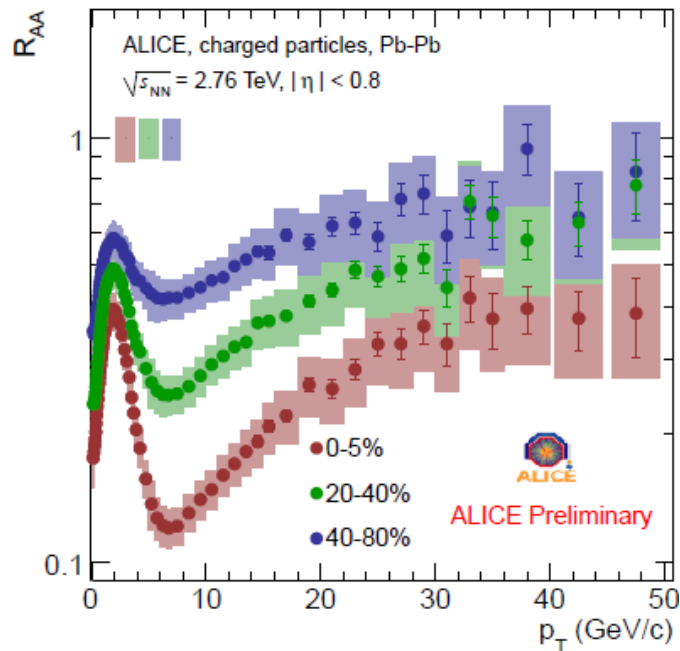
Figure 1.3: The nuclear modification factor from Pb-Pb collisions at $\sqrt{s} = 2,76$ TeV with different centralities [6].

ratio of the number of binary *NN* collisions [7]. At high momentum transfer p_T, there is a suppression of particle production which can be expressed in terms of the $R_{AA}(p_T)$. The hadron production suppression is due to energy loss as the hadrons transverse the QGP. By studying particle yields, like scaling *NN* collisions, for instance proton-proton collisions, by the number of nucleons corresponding to *AA* collisions and assuming there are no effects from the QGP, one would expect a unity in the ratio of the two particle yields. A reduced ratio however indicates a suppression. The R_{AA} spectra measured at ALICE from a Pb-Pb collision at $\sqrt{s} = 2,76$ TeV are shown in *Figure 1.3* where one clearly can see a suppression at $p_T \approx 7$ TeV followed by a rise as the p_T increases. This increase however is consistent with the expected behavior of the parton energy loss where the relative energy loss decreases as the p_T increases.

When comparing the R_{AA} distribution at high p_T for different hadrons and mesons, they all show the same suppressing behavior (see *Figure 1.4* for the case of *D* mesons). This implies that the dominating energy loss process is identified at a partonic level. If the hadronic energy loss were to be dominant, the different hadrons would have different corresponding cross sections depicting the different energy loss processes. The study of heavy flavor quark production in heavy ion collisions provides important information regarding energy loss at a partonic scale which in turn can provide information about the produced QCD matter. Heavy quarks are primarily produced in initial hard scattering processes, making them ideal probes since they undergo the entire evolution of the created QCD matter.
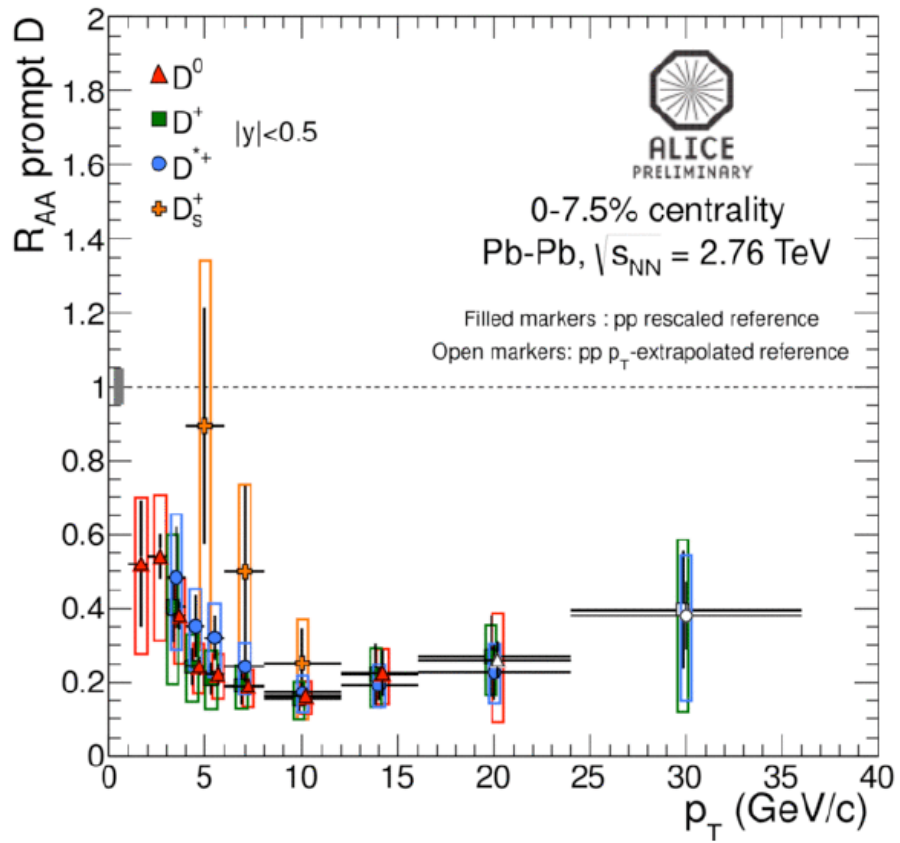
Figure 1.4: The R_{AA} from Pb-Pb collisions at $\sqrt{s} = 2,76$ TeV for D mesons at 0-7.5% centrality [8].

Chapter 2

LHC and ALICE

The Large Hadron Collider (LHC), located near Geneva, is CERN's (the European Organization for Nuclear Research) flagship when it comes to experimental particle and nuclear research. The LHC is a dual-ring hadron accelerator and collider built between 1998 and 2008. The 26.7 km tunnel in which it is installed was pre-existing and built between 1984 and 1989 for the LEP machine. The tunnel consists of eight straight sections as well as eight arcs, and lies roughly 100 m beneath the surface. There are currently seven detectors installed at the LHC, located in caverns at the intersection points of the accelerator. These are known as ATLAS, CMS, LHCb, TOTEM, MoEDAL, LHCf and ALICE. ATLAS and CMS are large multi-purpose detectors, while ALICE and LHCb are more specifically. TOTEM, MoEDAL and LHCf are for very special research purposes [9].

A particle collider where the particle beams counter-circulate and collide are far more superior to ordinary accelerators where a particle beam hits a stationary target when regarding particle production. The available energy used to produce particles in collisions is the center-of-mass (CMS) energy. For two colliding beams of particles, the CMS is the sum of the energies corresponding to the incoming beams. In the case of a collision with a fixed target, the CMS energy is proportional to the square root of the beam energy, meaning a beam collision is preferable regarding particle production.

The choice of hadrons as particle beams in collisions at the LHC is not random. In order to accelerate and collide the particles, the particle beams must be charged since magnets are the main contributor regarding beam manipulation. Also, unless needed, the particles can't decay which reduces the most prominent probes to be electrons, protons and ions as well as the corresponding anti-particles. However, as a result of synchrotron radiation, heavier particles have far less energy loss per orbit in accelerators compared to lighter particles. Therefore, in case of circular accelerators such as the LHC, heavy particles should be utilized in collisions in order to obtain the highest amount of energy.

Characterizing particles and determining their corresponding trajectories in order to reconstruct collisions is a major task for physicists. The track itself contains a great deal of information as the curvature of the tracks indicates the charge, momentum is directly proportional to the radius of curvature and the sudden appearance of two particles indicates a decay of a neutral particle just to name a few observable attributes. However, in order to detect these observables one is in dire need of some sort of detector.
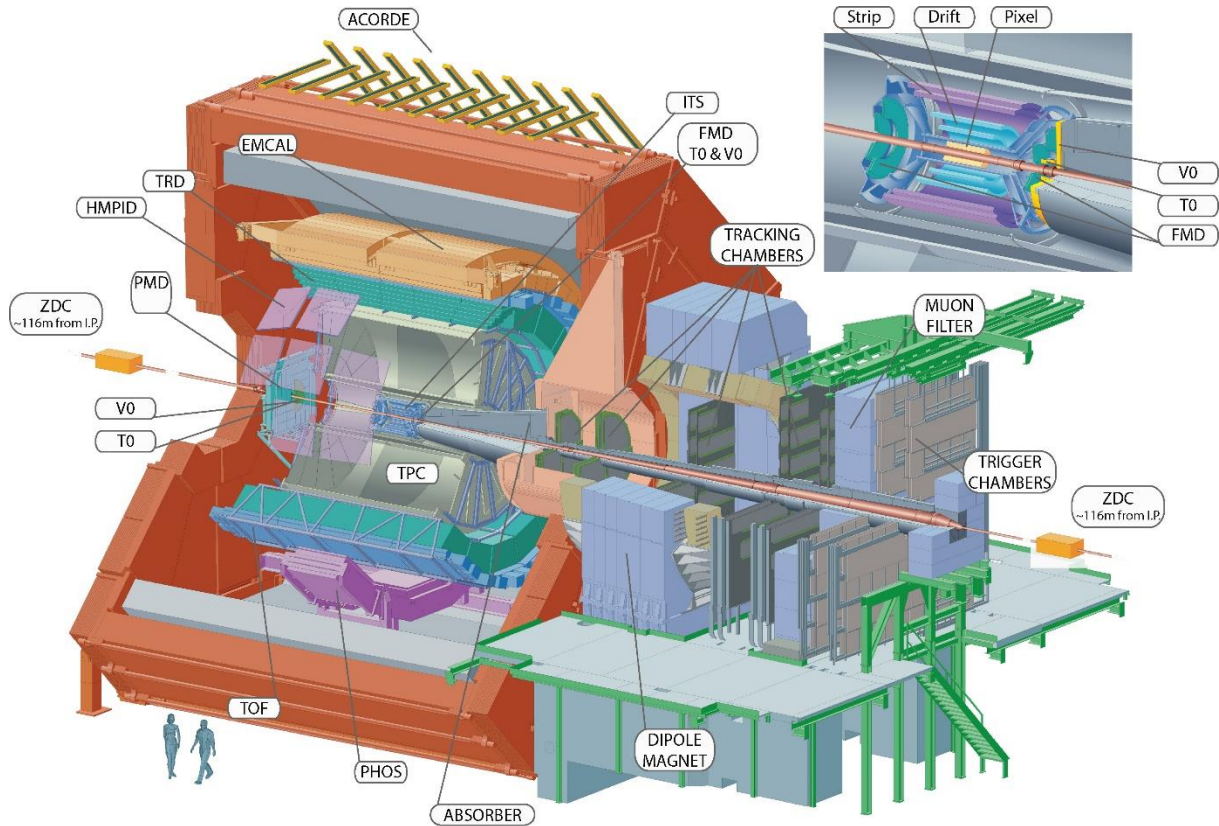
Figure 2.1: Schematic layout of the ALICE detector [10].

Particle detectors often consists of several layers of different detectors, where each sub-detector are specialized to specific observables. For instance, tracking detectors recreate particle trajectories, calorimeters measure energy deposits and particle identification devices combine several detectors and techniques in order to determine the identity of the particles.

2.1 The ALICE Detector

ALICE (A Large Ion Collider Experiment) is a heavy ion detector installed at the LHC with the general purpose of studying effects of strongly interacting quarks and gluons under extreme densities and temperatures originating from heavy nuclei collisions [11]. ALICE also enables the study of hadrons, muons, photons and electrons as well created in nucleus-nucleus collisions. Proton-proton collisions acts as reference modules for several heavy-ion collisions and QCD predictions.

The ALICE detector was built by a collaboration of over a thousand physicists and engineers from 30 different countries. The detector itself weighs approximately 10 000 tons with a dimension of $16 \times 16 \times 26 \text{ m}^3$. The detector focuses on physics at mid-rapidity, i.e., at low baryon and high energy densities and detects hadrons, leptons and photons.

2.2 ALICE Layout

The ALICE detector is located at Point 2 in the LHC. The detector is accessed by the PX24 shaft underneath the service building SX2 [12]. This, and the nearby buildings, acts as suppliers of gas, ventilation, cooling and electricity as well as other maintenance services. Equipment between the surface and the detector is transferred by a crane, capable of lifting 65 tons, located in the SX2 hall, where all detector operations are supervised as well. The particle beam pipe is located 44 m beneath SX2 in the cavern UX25, where ALICE is implemented.

The ALICE detector consists of 18 sub-detectors, each with a corresponding power supply, cooling system and data acquisition system. The central barrel of ALICE is surrounded by a solenoid magnet, named L3, with a length of 12.1 m and a diameter of 11.5 m. Enclosed inside L3 are the sub-detectors ITS, TPC, TOF, TRD, PHOS and EMCal. A dipole magnet, located 7 m from the interaction point, creates a magnetic field perpendicular to the particle beam and is an important part of the muon spectrometer. In the following sections, some of the sub-detectors will be discussed in more detail.

2.2.1 The Inner Tracking System (ITS)

The ITS is a sub-detector enclosing the particle beam pipe, consisting of cylindrical silicon detectors engulfed within a radius between 4.0 cm and 43.0 cm. The layers and their corresponding positioning are optimized for track determination and high impact-parameter resolutions, allowing the ITS to locate primary vertices with a resolution smaller than 100 µm.

In high-energy heavy nuclei collisions, one expects a very high particle density. In order to obtain a high resolution, six layers of silicon detectors are placed around the beam pipe. For the two inner-most layers, Silicon Pixel Detectors (SPD) are chosen, whereas Silicon Drift Detectors (SDD) contribute to the two following layers. The two outer-most layers are Silicon micro-Strip Detectors (SSD). The four outer-most silicon detectors provide energy loss measurements for low-momentum ionizing particles due to its analogue output in the non-relativistic region, turning the ITS into a low-p_T spectrometer.

The SPDs primary task is to determine vertex positions as well as measuring the impact parameter of tracks originating from decays of heavy quarks (charm, strange and beauty) and operates with a track density of 50 tracks/cm^2. The four next layers, consisting of the SDD and SSDs, are essential in particle identification by measuring energy deposits. The two outer-most layers are also in charge of matching the tracks between the ITS and the next sub-detector, the TPC.

2.2.2 The Time-Projection Chamber (TPC)

The main task of the TPC is to measure particle momentum distributions, provide particle identification and determine vertices. The TPC spans the entire azimuthal range, and covers a phase space of $|\eta| = 1.5$ for reduced tracks lengths and $|\eta| < 0.9$ for full track lengths. The transverse momentum range is covered from 10^{-1} GeV to 10^2 GeV. Inside the field cage, electrons are transported up to 2.50 m to one of the end plates. At each end plate, 18 separate trapezoidal units contains multi-wire proportional chambers, where each chamber are equipped with cathode pad readouts.

The TPC is a cylindrical in geometry with an inner radius of 0.85 m, an outer radius of 2.50 m and a length of 5.00 m. The field cage contains a central high-voltage electrode and two diagonally potential dividers which induce a uniform electrostatic field in the detector gas. The electrode is a 22 μm thick Mylar foil, placed approximately perpendicular to the beam axis. Aluminized Mylar strips, woven 18 times around support rods define the electric potential.

The field cage is filled with 90 m^3 of some detector gas, usually Ne, CO_2 or N_2. This choice of drift gas is not random, as they all have suitable properties regarding drift speed, radiation length as well as ageing and stability. In the case of Ne and CO_2 however, there is a very high dependence between the drift velocity and temperature which has led the TPC to keep a thermal stability with a maximum fluctuation of $\Delta T \leq 0.1$ K. The TPC also utilizes a gas envelope of CO_2 as insulation in vessels around the field cage.

As mentioned, the TPC uses multi-wire proportional chambers with cathode pad readout. The readout chambers are installed at the end plates of the TPC, which covers an area of 32.5 m^2. Due to the readout dependency of track density, the readout is radially segmented into sectors in two chambers with a slightly different geometry. In order to obtain the necessary energy deposit and track separation resolution, the TPC uses approximately 5.6×10^5 cathode pads in total.

2.2.3 The Time-Of-Flight (TOF) detector

The TOF detector operates in the central pseudo-rapidity region where its main priority is particle identification. The momentum range covers up to 4 GeV for protons and 2.5 GeV for kaons and pions, and combined with data from ITS and TPC the TOF is able to identify large particle samples as well as contribute invariant mass studies of kaons.

The detector is installed in a cylindrical frame with an internal radius of 3.70 m and an external radius of 3.99 m. The basic elements of the TOF detector are 1.22 m long and 0.13 m wide strips placed inside modules installed transversely to the particle beam axis. In total, the TOF detector consists of 90 modules, where the central modules contain 15 MRPC strips while the external modules consists of 19 strips.

2.2.4 The Photon Spectrometer (PHOS)

The PHOS is a single-arm high-resolution electromagnetic spectrometer with the main task of testing thermal properties from direct low p_T photon measurements as well as investigating jet quenching. The PHOS is installed at the very bottom of the ALICE detector, 4.60 m away from the center point of interaction and covers the entire azimuthal spectrum.

Each spectrometer module consists of 3.584 cells arranged in 56 rows containing 64 detection cells. The cells consists of lead-tungstate crystals coupled to an Avalanche Photo-Diode (APD). The APD and a preamplifier is glued to the end of a crystal, which are arranged in two rows of eight detection cells. The analog signals from this strip are connected to triggers through a T-shaped connector.

In order to increase the light yield from the tungstate crystals, the PHOS modules are kept at a steady temperature of $-25°C$. The temperature is monitored by temperature sensors installed between the crystals, with a thickness ranging from 30 to 50 μm. The PHOS detection cells are monitored by stable current generators and a system of Light Emitting Diodes.

2.2.5 The ElectroMagnetic Calorimeter (EMCal)

EMCal is a cylindrical Pb-scintillator calorimeter placed in opposite azimuth to the PHOS calorimeter and adjacent to the ALICE magnet coil. The positioning is due to the installation of PHOS below the TPC combined with the implementation of HMPID above the TPC, which renders EMCal to a region of 107° in azimuth above TPC.

Due to the large acceptance, which covers $|\eta| \leq 0.7$, EMCal provides a substantial increase to the electromagnetic calorimeter coverage in ALICE as well as fast triggers for hard jets, electrons and photons. Since EMCal measures neutral jet energies, full jet reconstructions are available for all collision systems.

EMCal is divided into 12.288 module towers, where each tower is grouped into two different super modules corresponding to the azimuthal acceptance. The super modules consists of 288 modules arranged in 24 strips, where each module are made up from alternating layers of 1.44 mm Pb and 1.76 mm polystyrene molded scintillators.

2.2.6 The Muon Spectrometer

The muon spectrometer operates in the pseudo-rapidity region $-4.0 < \eta < -2.5$, which corresponds to the polar angular range $171° - 178°$, with the main task of mapping vector-meson resonances in muon decays. At LHC energy scales, muons originating from semi-leptonic open charm and beauty decays dominate the particle yield, thus enabling a study of open heavy flavor production. The muon spectrometer consists of a front absorber, a tracking system, a dipole magnet, a muon-filter, trigger chambers and a beam shield.

The absorber's main task is to absorb hadrons and photons emerging from the interaction point. The absorber is installed inside the solenoid magnet with a length of 4.13 m. In order to limit the energy loss of the measured muons, the absorber is preponderantly made of carbon and concrete. A dense absorber, or tube shield, made of tungsten and stainless steel surrounds the beam pipe and acts as a shielding for the spectrometer. Finally, a muon filter, which is basically an iron wall with a thickness of 1.2 m, is placed in front of the trigger chambers for additional shielding.

The tracking chambers need a spatial resolution of 100 μm in order to cope with the invariant mass resolution of the Υ mass. In total, the tracking chambers of the muon spectrometer covers an area of 100 m^2 with a maximum hit density of 5×10^{-2} cm^{-2}. In order to meet these requirements, the spectrometer utilizes cathode pad chambers arranged in five stations. Two stations are installed in front of the dipole magnet, one is installed inside the dipole and two are placed behind the dipole. The stations consists of cathode planes which provides two-dimensional hit information.

2.2.7 The Zero Degree Calorimeter (ZDC)

By measuring the energy of non-interacting nucleons in the forward direction, that is, at 0° relative to the beam axis, an estimate of the number of participant nucleons can be determined. These spectator nucleons can be detected by ZDCs, which also provides centrality information and reaction plane estimates. There are two ZDCs installed in ALICE, both located 116 m on each side of the vertex point.

Non-interacting protons and neutrons are spatially separated by magnetic devices of the LHC beam pipe. The ZDCs therefore consists of two detectors; one for non-interacting protons and one for the neutrons. Both detectors are installed on lifts, enabling them to be lowered out of the beam plane when they are not used.

The ZDCs are quartz fiber Cherenkov calorimeters. When produced particle showers transverse dense absorbers, they emit Cherenkov radiation in the quartz fibers. Due to the innate velocity of the Cherenkov radiation emission, these calorimeters provides very fast signals. The absorbers consists of layers of 40 lead plates, each with a thickness of 3.0 mm, with quartz fibers placed between the plates. The fibers have a diameter with a thickness of 550 μm.

2.2.8 The Photon Multiplicity Detector (PMD)

The PMD measures photon multiplicity and spatial distribution in the pseudo-rapidity region $2.3 \leq \eta \leq 3.7$. By measuring photon multiplicity, one can establish important information regarding phase transitions, state of matter and chiral condensates. The PMD also yields information regarding the reaction plane.

2.2.9 The Forward Multiplicity Detector (FMD)

The FMD operates in the pseudo-rapidity range $-3.4 < \eta < -1.7$ and $1.7 < \eta < 5.0$ and provides charged-particle multiplicity information. There is an overlap between the FMD's silicon rings and ITS' inner pixel layer which acts as a cross check of measurements. The FMD also provides multiplicity fluctuation information on an even-by-event basis within the pseudo-rapidity range.

There are in total three FMD rings installed in ALICE. FMD2 and FMD3 consists of an inner ring and an outer ring of silicon sensors, located on each side of ITS. FMD1 is placed located further away from the vertex point in order to expand the charged particle multiplicity range.

2.2.10 The V0 Detector

The V0 detector consists of two arrays of scintillator counters placed on each side of the vertex point. The detector provides luminosity measurements in pp collisions as well as minimum-bias triggers.

The two scintillator counters are called V0A and V0C. The V0A is located 3.4 m away from the vertex opposite to the muon spectrometer while V0C is placed 0.9 m from the vertex point in front of the hadronic absorber. V0A covers the pseudo-rapidity range $2.8 < \eta < 5.1$ while V0C covers the range $-3.7 < \eta < -1.7$. The counters consists of a BC404 scintillating material and Wave-Length Shifting fibers with a diameter of 1 mm.

2.2.11 The T0 Detector

The T0 detector's main task is to provide trigger and timing signals. T0 has a detector dead time of 25 ns, corresponding to the order of the bunch crossing period in pp collisions. The detector also measures vertex positions for each interaction, yields centralities and delivers a "wake up" signal to TRD.

The detector contains two arrays, T0-A and T0-C, containing 12 Cherenkov counters. The counters are photomultipliers with a diameter of 30 mm and a diameter of 45 mm. The T0-A covers the pseudo-rapidity range $4.61 < \eta < 4.92$ while the T0-C covers the range $-3.28 < \eta < -2.97$. In order to maximize the trigger efficiency, the arrays are placed very close to the beam pipe. At 14 TeV, the trigger efficiency of T0 for minimum bias pp collisions is roughly 40%. However, due to the large multiplicities, the trigger efficiency in heavy-ion collisions is basically 100%.

2.2.12 The ALICE Cosmic Ray Detector (ACORDE)

ACORDE is an array of plastic scintillator modules installed on the surface of the L3 magnet in ALICE. Each module contains two scintillator counters and two PMTs at the end of the scintillators installed in an aluminum 40 kg structure. The modules provides fast trigger signals for calibration for different tracking detectors, but the main task is detecting atmospheric muons and muon bundles which allows for a study of high-energetic cosmic radiation.

In total, ACORDE contails 60 scintillator counters. Each time atmospheric muon interacts with the detector, ACORDE sends a fast trigger signal to the Central Trigger Processor. This signal is also used by TPC, ITS, TOF and HMPID as performance tests. The rate at which a single atmospheric muon hits ACORDE is around 4.5 Hz/m^2 at the very top of L3 and need at least an energy of 17 GeV in order to reach the detector barrel. However, since the upper limit for reconstructing muon tracks in TPC is around 2 TeV, this will allow measurements of muon momentum spectra in a very wide range.

Chapter 3

The ALICE Offline Framework

The main task of the ALICE offline framework is to finalize the experimental activity by interpreting the actual results. This includes reconstruction, calibration, analysis and simulation of data. In this chapter, the ALICE offline framework, AliRoot, will be discussed in detail, followed by a section describing the constituents of an ALICE analysis task.

3.1 The AliRoot Framework

AliRoot is an Object-Oriented software framework based on the ROOT system [13]. The AliRoot framework contains several different event generators, particle transport packages and when supplemented by AliEn enabled access to Grid computing. The main task of the AliRoot framework is analysis, simulation and reconstruction of the experimental data. A schematic view of how the framework is constructed can be seen in *Figure 3.1*.

The main interactions in an event are simulated using event generators. The event generator creates particles with different momenta, which is used in the study of the production history, i.e. the production vertex and decay. This is the base for the Kinetic tree, which is used in transport packages such as GEANT3 and FLUKA. The transport packages, as the name implies, transports the simulated particles through the different detectors and produces hits. Hits are energy deposits at a given point in space and time, and also contains track labels from the particles which created the hits. The hits can be viewed as the energy deposit in the whole volume of the active detector, as in the case of calorimeters, or merely as a matter of comparison in detectors like TOF.

From the hits we can create digits. The transition from hits to digits are given by a disintegrated response, meaning we strip, or disintegrate, the tracks and only let the labels contain the Monte Carlo simulation information. The digits can also be split into the categories summable digits and digits. The summable digits makes use of low thresholds and carries an additive result, whereas the digits uses real thresholds similar to the actual data. There are however a few differences between the digits and the raw data produced by the detectors. For instance, the raw data is stored in a ROOT structure whilst the digits are stored in a class. With the digits, one can use reconstruction chains to study both the software and detector performance, making use of either real or simulated data.
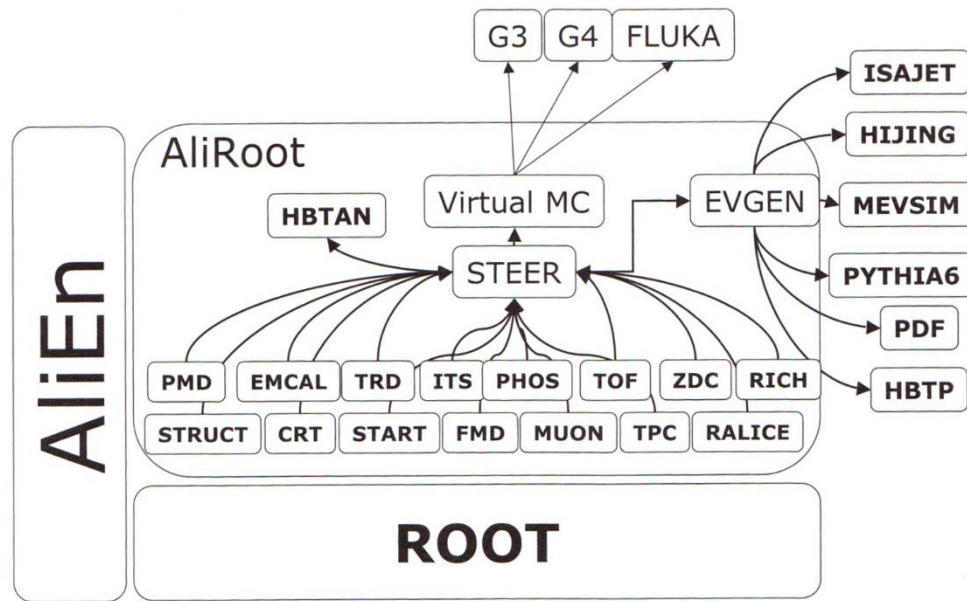
Figure 3.1: A schematic view of AliRoot and its constituents [14].

3.1.1 Simulation

The tremendous amount of particles created in heavy ion collisions at GeV energy scales gives birth to a series of problems when dealing with reconstruction and analysis. The accuracy of the detectors are dependent on simulation algorithms of the detector response, therefore simulation is a crucial step regarding calibration of detectors.

Simulation processes include the generation of the initial particle packages, production and decay from the interactions and the particle transport through the detectors. The AliROOT framework is capable of simulating collisions, generate particles created in the collisions and simulate hits as the particles traversing detectors. The particles created in collisions are produced by generators, such as AliGenerator. The class AliDecayerPythia is responsible for the decay simulation of particles. The simulation is prepared using the macro Config.C, a C++ macro which configures the Monte Carlo simulation, magnetic fields and detectors etc.

The class TVirtualMC is the foundation regarding how the particles traverse the detectors, while TGeo defines different geometry properties of the detectors, alongside the functions CreateMaterials, BuildGeometry and CreateGeometry. AliDetector, a subclass of AliModule, is responsible for the active modules, and AliModule and AliDetector creates the foundation for an interface to the simulation software. High-

15

energy proton-proton collisions, interactions, fragmentations and jets are simulated using Pythia. The PHOJET generator implements the Dual parton model in pp collisions, combining Regge theory and pQCD in order to describe hard scattering processes [15]. The jet fragmentation simulations are created using HIJING (Heavy-Ion Jet Interaction Generator). This model is basically a hybrid of QCD-jet fragmentation theory and the Lund model, and is exceptionally accurate when dealing with small fragmentation ratios at intermediate energies. One of the more outstanding properties of the HIJING model is the prediction of nuclear shadowing. Nuclear shadowing is a model depicting how the eigenstates of free partons distributed in the nucleus changes. Due to nuclear shadowing, the multiplicity decreases at low parton momentum fractions.

MevSim is a simulation software, originally written in FORTRAN and later built into the AliROOT framework, created in order to produce nucleus-nucleus collisions in specific cases. The software run simulations according to the user's choice of number of particles, multiplicity fluctuations, number of events etc. MevSim is the base for GevSim, an event Monte Carlo generator used in testing algorithms and performance of detectors. GevSim uses distribution functions when generating particles, again based upon input the user chooses. However, GevSim is also capable of simulating event-by-event fluctuations, which provides an additional option for user defined distribution fluctuations alongside the distributions from MevSim.

3.1.2 Reconstruction

The reconstruction framework uses digits, often in ROOT tree format, inherited from the simulation framework as input. From the digits, clusters are reconstructed for each detector from which tracks and vertexes are determined. Each detector contributes a reconstructor class. The class AliReconstructor points AliReconstruction to the proper detector reconstruction class, which reconstructs detectors via plug-ins.

Local reconstruction is the first part of the reconstruction process. Each detector independently creates clusters, hence this process is often called clusterization. Using Reconstruct on the object that is to be reconstructed starts the local reconstruction, where all detectors run the local reconstruction. It is however possible to convert the raw data digits to a tree and use this digits tree as input instead of invoking the local reconstruction on the actual raw data. Reconstructions of vertexes in ALICE are based upon information given by the silicon pixel detectors. The algorithm from which the reconstruction of the vertexes are done begins with determining the distribution of space points in the z-direction in the first of the silicon pixel layers. A symmetric distribution implies the vertex having the z-coordinate $z = 0$, and an increased number of hits vanishes as the vertex position differs from the centroid. If the primary vertex location don't stray too far away from $z = 0$, usually up to $\sim$12 cm, the centroid is still reciprocally related to the actual vertex space point. The primary vertex is reconstructed by an object derived from AliVertexer. When all the local reconstructions are done for each separate detector, the method FindVertexForCurrentEvent is invoked, returning AliESDVertex.

Since each detector creates a separate set of information, one could easily see the need to combine all track reconstructions in order to achieve a single, optimal reconstruction track. The class AliESDTrack grants the detectors the ability to exchange data without neglecting the independencies of the different detectors. In order to achieve this possibility, AliESDTrack transform the information into a set of pointers, consisting merely of integers, to the tracks, thus allowing reconstruction of the needed tracks. Every section of the reconstruction framework for the tracking detectors utilize the same coordination set-up;

- Right handed coordinate system
- Cartesian coordinate system
- The detectors sensory plane is perpendicular to the x-plane
- The origin and z-axis coincide with a universal ALICE coordinate system

By choosing this set-up, the reconstruction calculations are greatly improved regarding simplicity. Transformations from local to global coordinate systems become way less tedious since these transformations merely become rotations around the z-axis. The final product output of the reconstruction framework is the Event Summary Data, or ESD.

3.1.3 Tracking

The actual tracking process consists of several steps. First, the tracking starts at the best tracking detector, where also the track density is at its minimum, namely the outer-most area of the TPC. The seeds, or the tracking objects, consists of a few number of clusters, therefore an extrapolation of the tracks to other detectors will contain a relatively large uncertainty. In order to minimalize the uncertainties, the tracking process is constrained within the TPC towards the inner-most part of the TPC. Each time new clusters are recognized as a part of a track, they are added making the tracking process more and more accurate. This process is done throughout the entire registry of the TPC, and is followed by a similar process in ITS. However, in addition to adding seed parameters, a unique ITS tracking system is available for the ITS clusters, enabling the ITS tracking system to detect tracks not found by the TPC due to decays etc.

When the tracking process reaches the inner-most part of the ITS, the tracking process starts all over again, back to the outer-most part of ITS and then again through the TPC. Using the potential tracks, time-of-flight hypotheses are made which the TOF uses for particle identification, PID. At this point, the parameters should contain an acceptable certainty and thus making extrapolation to the TOF, PHOS and TRD detectors available. In the TRD, the tracking process is quite similar to that of TPC. Track parameters are added as the track goes from the outer-most wall to the inner-most, saving clusters and improving the parameters until the information is sufficient for further extrapolation to TOF and PHOS. The tracking process finishes by a final refitting using the Kalman filter, yielding a remarkable accurate series of track parameters. The finalized series of reconstructed tracks, along with the particle information, are stored in the ESD. The Event Summary Data is analyzed using the class AliESD. The ESD contains information regarding event identification parameters (such as event number, time stamp, trigger cluster etc.),

ZDC energies, vertex positions, track multiplicity, interaction time, tracks and clusters. The ESDs are essential for analysis due to all the information stored in these files.

3.2 The ALICE Analysis Framework

The ALICE analysis framework enables an efficient way of processing ALICE data by utilizing parallel computing and providing data to different analysis modules simultaneously [26]. An analysis task, which is a ROOT macro, must be created in order to run an analysis algorithm using the ALICE analysis framework.

Usually, an analysis task derives from the class AliAnalysisTaskSE which implements a compliant communication between the analysis manager object and the data handlers. The mandatory objects needed in an analysis task are:

- *UserCreateOutputObjects( )*
  This method calls the output objects which are to be written of the analysis, i.e. histograms, trees etc.

- *UserExec( )*
  The UserExec( ) is where the user defines the actual analysis algorithm which is to be implemented. Input data usually consists of the type AliVEvent which is accessed via the fInputEvent member. For ESD analysis, the pointer must be directed to AliESDEvent, while MC information is accessed by the fMCEvent. Following is an example of a UserExec( ) which plots the p_T distribution of charmed particles.

- *Constructors( )*
  The constructors are needed in order to initialize the data members of the analysis task. The tasks must also contain a non-default constructor which defines the input and output slots of the analysis.

- *Data containers*
  Within the analysis task there exists predefined objects which define the different data types included in the analysis known as data containers. The data containers are never created within the analysis, but rather created by the means of a handling manager which puts together the analysis task. The main task of containers is to state the input and output data types. Usually, the input and output containers are created by connecting the input and output event handlers to managers.

Alongside the mandatory objects needed in order to successfully run an analysis task, there are several optional methods that can be added by the users for further simplicity. These include, but by far not limited to, *LocalInit( )*, *Notify( )* and *Terminate( )*. The latter is where the user usually chooses to draw the output.

Chapter 4

Heavy Flavor Quark Production

The study of particle energy loss is an essential means when determining properties of matter. At a partonic scale, quarks acts as brilliant probes due to their small extension as well as their wide range in mass, where the lightest quark, the up quark, has a mass of a few MeV whilst the most massive, the top quark, has a mass of approximately 173 GeV. Since quark flavor is conserved in hard interactions, the energy needed to produce a quark pair equals twice the mass of the quark of interest [16].

Quark pairs are produced in high-energy particle collisions, for instance proton-proton collisions, using large particle accelerators such as the LHC. However, by colliding heavy nuclei one can alongside the actual quark production obtain information regarding the energy loss of quark probes in the created QGP matter [17]. We can thus use the proton-proton collision as a reference and study the scaling to nucleus-nucleus collisions. Any suppression of created hadrons could thus be connected to energy loss due to the interaction between the quarks and the QGP. By studying heavy flavor electrons, one can map energy loss distributions and also distinguish charm and beauty flavors using electron-D^0 correlations.

There are three leading order heavy flavor quark production processes which arises in proton-proton collisions, known as flavor creation, flavor excitation and gluon splitting. Albeit we differ between these main production channels, the names could be somewhat misleading since all topologies accommodate the $g \rightarrow Q\bar{Q}$ vertex. In the following sections, a brief summary of some results of QCD will be presented as well as a deliberation of each production topology.

4.1 Quantum ChromoDynamics

Quantum ChromoDynamics, or QCD, is the gauge theory inferring color charge interactions. All hadrons are bound states of fermions known as quarks, where each quark is characterized by different masses and a fractional electric charge. Baryons are bound states of three so-called valence quarks, while mesons are assumed to be a bound quark-antiquark state. Although this hadron model can yield a remarkable description of the spectra of hadrons, there are two fundamental issues. First off there have yet to been

observed free quarks. Quarks always come in bound states due to the confinement principle. Secondly, there is a violation of the Pauli principle when looking at baryons like the Ω^--baryon, which apparently consist of three identical quarks with symmetric wave functions.

However, both phenomena can be explained by introducing gauge color theory, as proposed by Nambu and Greenberg in 1964. By introducing a new attribute to quarks, known as color, we assume that all quarks can exist in three different color states. Quark wave functions can thus be expressed as a product of a spin term and a color wave function, i.e.

$$\Psi = \psi \chi^c, \tag{4.1}$$

where ψ denotes spin and χ^c corresponds to the color wave function [18]. The QCD Lagriangian density is given by

$$\mathcal{L}_{QCD}(x) = \sum_{fl} \bar{\psi}_{fl}(x)[i\gamma^\mu D_\mu - m_{fl}]\psi_{fl}(x) - \frac{1}{4}\sum_{a=1}^{8} F^a_{\mu\nu}(x)F^{a\mu\nu}(x), \tag{4.2}$$

where the sum runs over all quark flavors and $F^a_{\mu\nu}(x)$ is the gluon field tensor. The covariant derivative is given by

$$D_\mu = \partial_\mu + igA_\mu(x) = \partial_\mu + ig\sum_{a=1}^{8} T^a A^a_\mu(x). \tag{4.3}$$

a corresponds to the eight gluon charges, g is the QCD coupling constant and T^a is an SU(3) generator satisfying the commutation relation

$$[T^a, T^b] = if^{abc}T^c \tag{4.4}$$

where f^{abc} are QCD structure constants. The gluon field tensor is given by

$$F^{\mu\nu}_a = \partial^\nu A^\mu_a - \partial^\mu A^\nu_a + gf_{abc}A^\mu_b A^\nu_c. \tag{4.5}$$

According to first-order QCD perturbation theory, the interaction Lagrangian consists of various combinations of quark and gluon fields. This property infer different vertex factors corresponding to the different interaction terms. For instance, a quark-gluon vertex (see *Figure 4.1*) yields the contribution

$$-ig\gamma^\mu(T^k)_{lm}. \tag{4.6}$$

A second term depicting a three-gluon vertex arises from second order field tensor terms, contributing a vertex factor given by

$$gf^{bcd}[g_{\nu\tau}(k_3 - k_2)_\sigma + g_{\tau\sigma}(k_2 - k_1) + g_{\sigma\nu}(k_1 - k_3)_\tau], \tag{4.7}$$

where τ and ν are some dummy indices. The third term from the interaction Lagrangian depicts a four-gluon vertex, contributing a vertex factor of

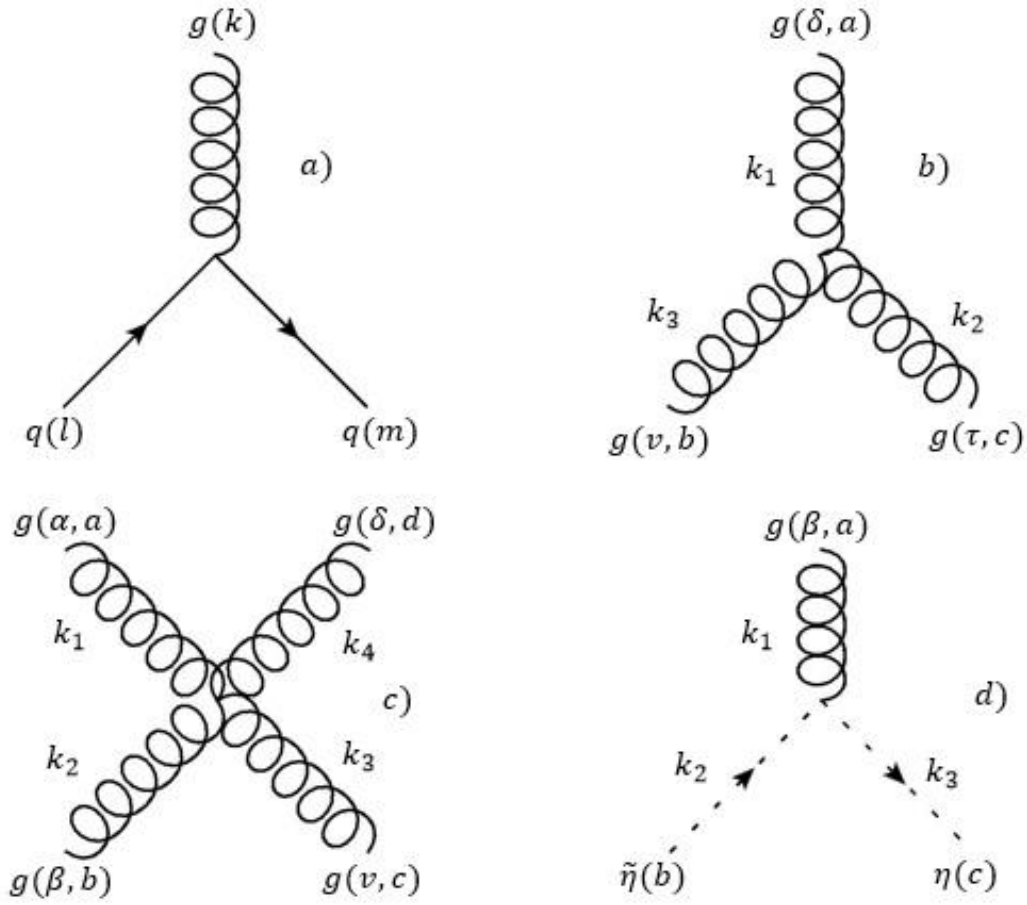$$-ig^2 G_{\alpha\beta\gamma\delta}, \tag{4.8}$$

Figure 4.1: The QCD vertex factors, where a) – d) corresponds to Eqs. (4.6), (4.7), (4.8) and (4.10).

where

$$G_{\alpha\beta\gamma\delta} = f^{kab}f^{kcd}\left(g_{\alpha\gamma}g_{\beta\delta} - g_{\beta\gamma}g_{\alpha\delta}\right) + f^{kcb}f^{kad}\left(g_{\gamma\alpha}g_{\beta\delta} - g_{\beta\alpha}g_{\gamma\delta}\right)$$
$$+ f^{kac}f^{kbd}\left(g_{\alpha\beta}g_{\gamma\delta} - g_{\gamma\beta}g_{\alpha\delta}\right). \tag{4.9}$$

The final term represents the ghost-gluon vertex, and contributes the factor

$$gf_{abc}k_2. \tag{4.10}$$

One of the more intriguing aspects of QCD arises when studying higher-order radiative corrections. By inducing renormalization, a renormalization of the coupling constant also emerges. From these corrections it can be shown that the renormalized coupling can be written as [19]

$$g_r = g_0\mu^{-\eta 2}\left[1 + \frac{g_r^2}{32\pi^2}\left(11 - \frac{2n_f}{3}\right)\left[\frac{2}{\eta} - \gamma + \ln 4\pi\right] + \mathcal{O}(g_r^4)\right]. \tag{4.11}$$

An interesting feature is how g_r decreases as μ increases. This particular property is usually expressed as

$$\alpha_s(\mu) \equiv g_r^2/4\pi \, , \tag{4.12}$$

defined in strict analogy to the fine-structure constant $\alpha \approx 137^{-1}$. The dependence of μ is usually expressed as

$$\alpha_s(\mu) = \frac{\alpha_s(\mu_0)}{1 + (\beta_0/4\pi)\alpha_s(\mu_0)\ln(\mu^2/\mu_0^2)} \, , \tag{4.13}$$

where we have defined

$$\beta_0 \equiv 11 - 2n_f/3 \, . \tag{4.14}$$

$\alpha_s(\mu_0)$ is a parameter determined experimentally. Current experiments suggests that the most precise value obtained so far is

$$\alpha_s(\mu_0 = m_Z = 91.21 \; GeV) = 0.118 \pm 0.002 \, . \tag{4.15}$$

Note that as μ decreases, α_s becomes larger. This is a very important result in QCD known as asymptotic freedom [20], a feature which plays a vital role in particle production mechanics.

4.2 Flavor Creation

The flavor creation process, or pair creation, occurs when two light quarks originating from two different hadrons collide, annihilate and produce a heavy quark pair. This can also however occur by gluon fusion, where two incoming gluons create the heavy quark pair [21]. The light quark annihilation process dominates for $2M_Q/\sqrt{s} \gg 10^{-1}$, whilst the gluon fusion process dominates for $2M_Q/\sqrt{s} \ll 10^{-1}$. Different Feynman topologies are shown in *Figure 4.2*. Referring to the Feynman diagram in *Figure 4.2 a)*, the Feynman amplitude is given by

$$\mathcal{M} = \frac{ig^2}{4\hat{s}} (\gamma^\mu)_{\beta\alpha} (\gamma_\mu)_{\gamma\delta} (\lambda^k)_{ba} (\lambda^k)_{cd}, \tag{4.16}$$

where $(\lambda^k)_{ij}$ are the Gell-Mann matrices, Greek subscripts denote spin, Latin subscripts denote color charge and $\hat{s} = Q^2$. Squaring the matrix element, summing over all spin and color and integrating over $\hat{t} = (p_1 - p_3)^2$ we find

$$\sigma_{q\bar{q} \to Q\bar{Q}}(\hat{s}) = \frac{8\pi\alpha^2(Q^2)}{27\hat{s}^2} \left(\hat{s} + 2M_Q^2\right) \sqrt{1 - \frac{4M_Q^2}{\hat{s}}} \, . \tag{4.17}$$
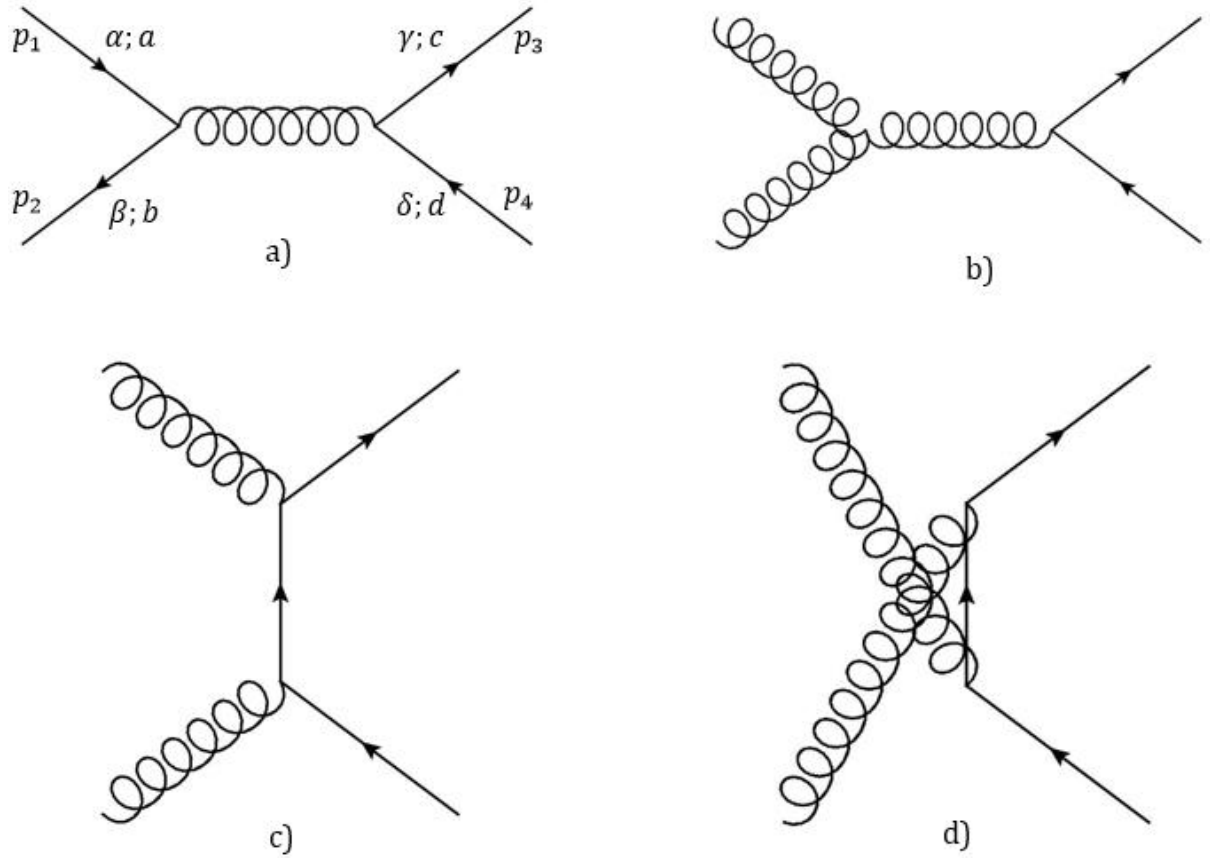
*Figure 4.2: Feynman topologies for the flavor creation processes. a) refers to
$q\bar{q} \to Q\bar{Q}$, b) – d) refers to $gg \to Q\bar{Q}$.*

In the gluon fusion processes, referring to Figure *4.2 b) – d)*, the Feynman amplitude is given by

$$
\mathcal{M} = \frac{ig^2}{4} \left\{ \frac{1}{2} [\lambda_a, \lambda_b]_{cd} \left(g^{\alpha\beta} (\not{p}_2 - \not{p}_1) + 2\gamma^\alpha p_1 - 2\gamma^\beta p_2 \right)_{\gamma\delta} \right.
$$

$$
+ \frac{1}{M_Q^2 - \hat{t}} (\lambda^a \lambda^b)_{cd} \left(\gamma^\alpha (\not{p}_3 - \not{p}_1 + M_Q) \gamma^\beta \right)_{\gamma\delta}
$$

$$
\left. + \frac{1}{M_Q^2 - \hat{u}} (\lambda^b \lambda^a)_{cd} \left(\gamma^\beta (\not{p}_3 - \not{p}_2 + M_Q) \gamma^\alpha \right)_{\gamma\delta} \right\}, \qquad (4.18)
$$

where $\hat{t} = (p_1 - p_3)^2$ and $\hat{u} = (p_1 - p_4)^2$. Squaring the amplitude and summing over spin and color finally yields the cross section given by

$$\sigma_{gg \to Q\bar{Q}}(\hat{s}) = \frac{\pi \alpha^2(Q^2)}{3\hat{s}} \left[-\left(7 + \frac{31 M_Q^2}{\hat{s}} \right) \frac{1}{4} \Gamma + \left(1 + \frac{4 M_Q^2}{\hat{s}} + \frac{M_Q^4}{\hat{s}^2} \right) \log \frac{1 + \Gamma}{1 - \Gamma} \right], \quad (4.19)$$

where

$$\Gamma = \sqrt{1 - \frac{4 M_Q^2}{\hat{s}}}. \qquad (4.20)$$

It should be noted that in the case of flavor creation, the created parton showers do not alter any cross sections regarding production yield. The only modification is purely kinematic as the produced heavy quark pair must emerge in azimuth in order to avoid violation of momentum.

4.3 Flavor Excitation

In the flavor excitation process, a heavy sea quark belonging to an incoming hadron scatters off a quark or a gluon from the other hadron. Referring to *Figure 4.3 a)*, the Feynman amplitude for the excitation process $qQ \to qQ$ squared and summarized over all spin and momenta is given by

$$\sum |\mathcal{M}_{qQ \to qQ}|^2 = \frac{64}{9} \pi^2 \alpha^2(Q^2) \frac{\left(M_Q^2 - \hat{u}^2 \right)^2 + \left(\hat{s} - M_Q^2 \right)^2 + 2 M_Q^2 \hat{t}}{\hat{t}^2}. \qquad (4.21)$$

In the case of the topologies given by *Figure 4.3 b) – d)*, the Feynman amplitude can be expressed as

$$\begin{aligned}
\sum |\mathcal{M}_{gQ \to gQ}|^2 = \pi^2 \alpha^2(Q^2) \Bigg\{ &\frac{32 \left(\hat{s} - M_Q^2 \right) \left(M_Q^2 - \hat{u} \right)}{\hat{t}^2} \\
&+ \frac{64}{9} \frac{\left(\hat{s} - M_Q^2 \right) \left(M_Q^2 - \hat{u} \right) + 2 M_Q^2 \left(\hat{s} + M_Q^2 \right)}{\left(\hat{s} - M_Q^2 \right)^2} \\
&+ \frac{64}{9} \frac{\left(\hat{s} - M_Q^2 \right) \left(M_Q^2 - \hat{u} \right) + 2 M_Q^2 \left(M_Q^2 + \hat{u} \right)}{\left(M_Q^2 - \hat{u} \right)^2} + \frac{16}{9} \frac{M_Q^2 (4 M_Q^2 - \hat{t})}{(\hat{s} - M_Q^2)(M_Q^2 - \hat{u})} \\
&+ 16 \frac{\left(\hat{s} - M_Q^2 \right) \left(M_Q^2 - \hat{u} \right) + M_Q^2 (\hat{s} - \hat{u})}{\hat{t}(\hat{s} - M_Q^2)} \\
&- 16 \frac{\left(\hat{s} - M_Q^2 \right) \left(M_Q^2 - \hat{u} \right) - M_Q^2 (\hat{s} - \hat{u})}{\hat{t}(M_Q^2 - \hat{u})} \Bigg\}.
\end{aligned} \qquad (4.22)$$

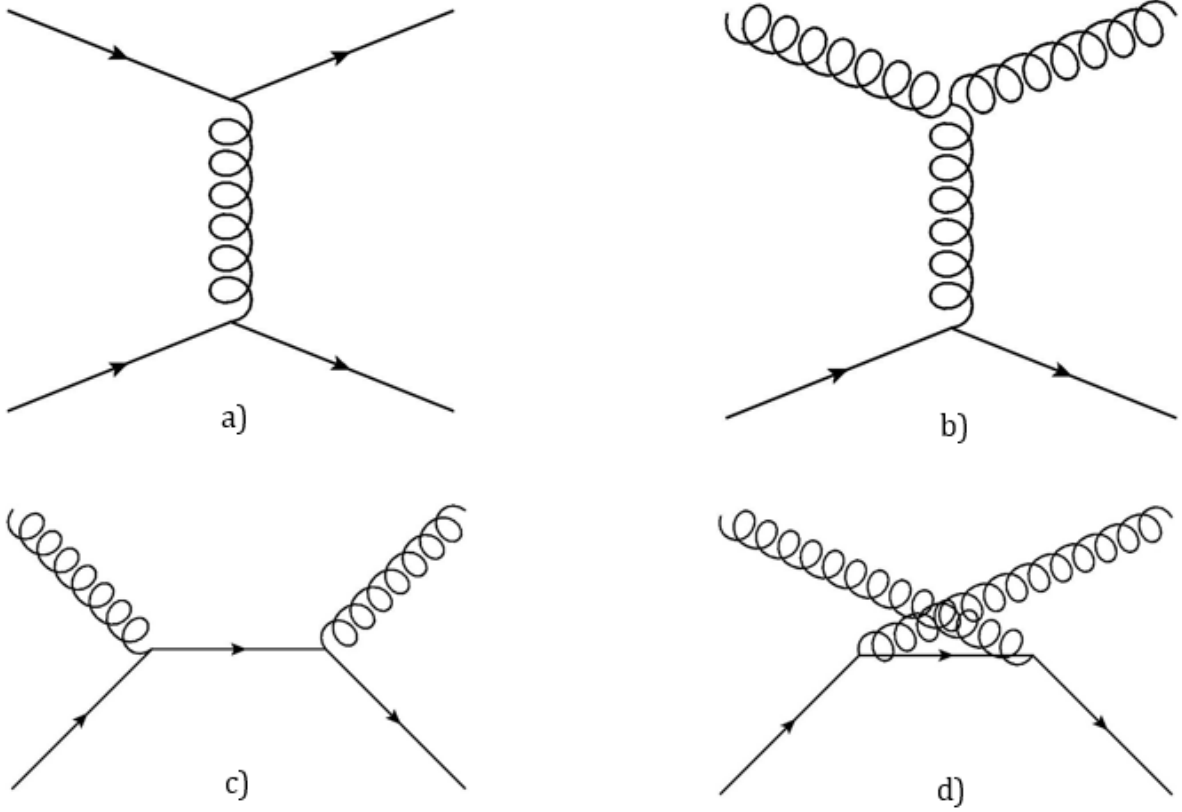*Figure 4.3: Different Feynman diagrams depicting the flavor excitation process. a) refers to $qQ \to qQ$, b) – d) refers to the process $gQ \to gQ$.*

The production cross section is given by

$$\hat{\sigma} = \frac{1}{16\pi\left(s - M_Q^2\right)^2} \int dt \sum |\mathcal{M}|^2 \ ,$$ (4.23)

which upon very intricate and tedious integration yields

$$\hat{\sigma}_{qQ \to qQ}(\hat{s}) = \frac{4\pi\alpha^2(Q^2)}{9\left(\hat{s} - M_Q^2\right)^2}\left[\left(1 + \frac{2\hat{s}}{Q_0^2}\right)\left(\frac{\left(\hat{s} - M_Q^2\right)^2}{\hat{s}} - Q_0^2\right) - 2\hat{s}\log\frac{\left(\hat{s} - M_Q^2\right)^2}{Q_0^2\hat{s}}\right] \ ,$$ (4.24)

where we have chosen $Q_0^2 = -t$. Likewise, we find

$$
\hat{\sigma}_{gQ \to gQ}(\hat{s}) = \frac{\pi \alpha^2(Q^2)}{(\hat{s} - M_Q^2)^2} \left[\left(1 + \frac{4}{9} \left\{ \frac{\hat{s} + M_Q^2}{\hat{s} - M_Q^2} \right\}^2 \right)(L - Q_0^2) + \frac{2}{9} \frac{(Q_0^4 - L^2)}{(\hat{s} - M_Q^2)} + 2(\hat{s} + M_Q^2) \log \frac{Q_0^2}{L} \right.
$$

$$
+ \frac{4}{9} \frac{\hat{s}^2 - 6M_Q^2 \hat{s} + 6M_Q^4}{\hat{s} - M_Q^2} \log \frac{\hat{s} - M_Q^2 - Q_0^2}{\hat{s} - M_Q^2 - L} + 2(\hat{s} - M_Q^2)^2 \left(\frac{1}{Q_0^2} - \frac{1}{L} \right)
$$

$$
\left. + \frac{16}{9} M_Q^4 \left(\frac{1}{\hat{s} - M_Q^2 - L} - \frac{1}{\hat{s} - M_Q^2 - Q_0^2} \right) \right],
\tag{4.25}
$$

with the term L given by

$$
L = \min \left(\hat{s} - M_Q^2 - Q_0^2, \frac{(\hat{s} - M_Q^2)^2}{\hat{s}} \right).
\tag{4.26}
$$

It should be mentioned that if the heavy quark is not a valence quark, it originates from a gluon splitting branching along the parton distribution time-line. According to parton distribution parameterizations, heavy flavor production yields vanishes at $Q^2 < m_q^2$. This implies that hard scattering processes has a virtuality above the threshold m_q^2, meaning a reconstruction of any initial state parton shower will contain the branching $g \to Q\bar{Q}$ given $Q_0^2 < m_Q^2$, where Q_0 denotes the lower parton shower cut-off. As a consequence, the production mechanism instead becomes $gq \to Q\bar{Q}g$ or $gg \to Q\bar{Q}q$ [22].

4.4 Gluon Splitting

Gluon splitting refers to the vertex branch $g \to Q\bar{Q}$, as seen in *Figure 4.4 a)*, in either the initial state or final state parton shower where no heavy flavor quarks attend any hard scattering processes. Most initial state gluon splitting topologies abates to the previously-covered flavor excitation mechanism. An equivocation can be seen in the topology given by *Figure 4.4 b)* where a gluon first branches to a $Q\bar{Q}$-pair and the emerging Q later emits another gluon which is to enter a hard scattering process. Although this technically can be considered as a flavor excitation mechanism, it is custom to accredit this process gluon splitting since the hard scattering process don't encompass heavy flavors.
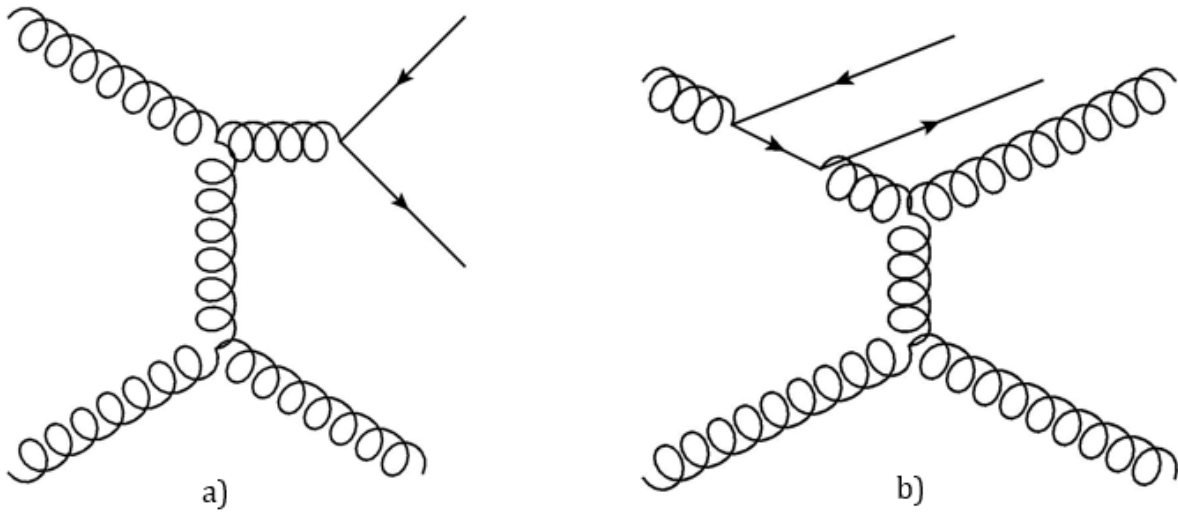
Figure 4.4: Examples of gluon splitting heavy flavor production topologies.

4.5 Succinct

All three production mechanisms, i.e. creation, excitation and splitting, can be distinguished by having 2, 1 or 0 heavy flavors in the final state of the hard scattering process. At small energies, the flavor creation mechanism is the dominating process, followed by a small contribution from flavor excitation and a negligible gluon splitting contribution. Increasing the energy enhances excitation and splitting contribution until the excitation process overtakes the flavor creation mechanism. It should be noted that the decay of heavy resonances, such as $Z^0 \to b\bar{b}$ or $W^+ \to c\bar{s}$, contributes to the production of heavy flavors. However, these processes will not be covered in this thesis.

One should keep in mind that total cross sections are rarely measured, but instead determined by extrapolation of measurements, a feature which could infer a potential bias. The differential cross sections however are a lot harder to predict since quantities at different scales in QCD induce large perturbative expansion logarithms, implying the need of resummations. In principle, one could write the measured differential cross section as

$$\frac{d\sigma_H}{dp_T} = \frac{d\sigma_Q}{dp_T} \otimes F^m \,, \tag{4.27}$$

where the first constituent represent NLO and NLL calculations and the second term correspond to a non-perturbative fragmentation F^m which can be determined experimentally. *Figure 4.5* depicts beauty production from electron-positron annihilation. The non-perturbative contribution F^m can be written as

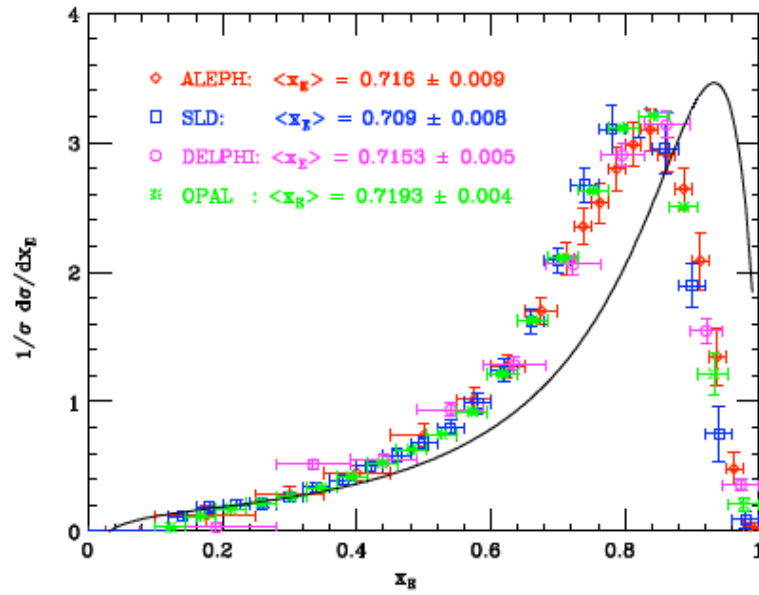$$F^m = \frac{measurements}{pQCD \; predictions} \,. \tag{4.28}$$

Figure 4.5: Beauty production from electron-positron annihilation as a function of the Bjorken x. The colored indices indicate measurements, the line corresponds to pQCD predictions [23].
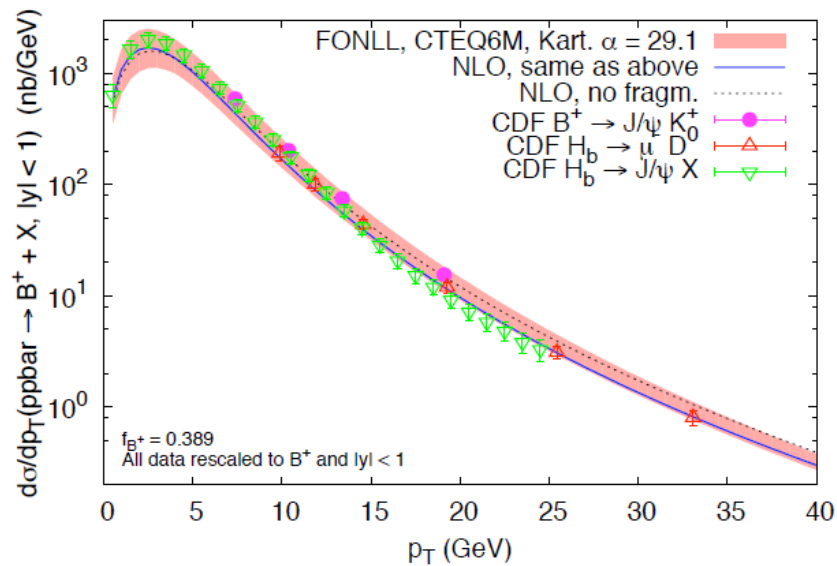

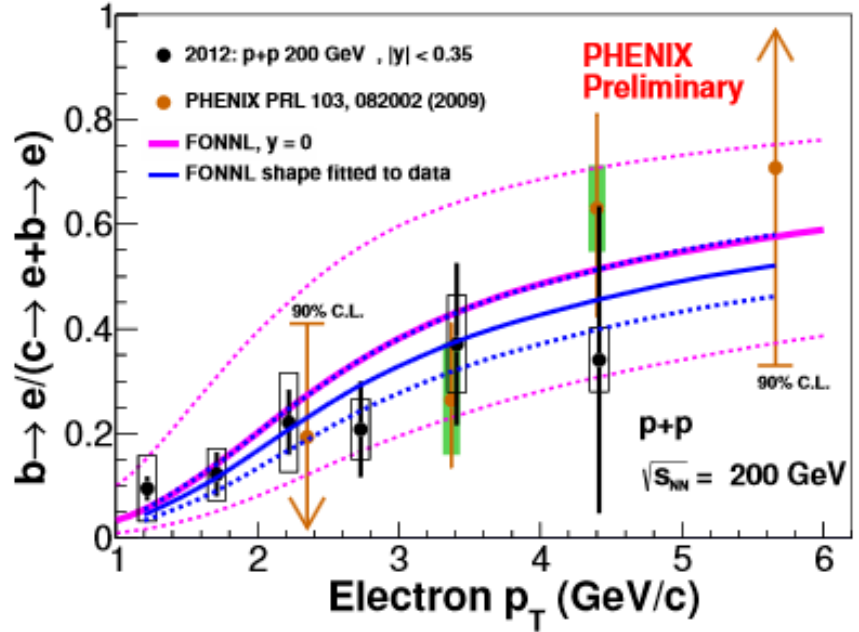*Figure 4.6: Beauty differential cross section from p-p̄ collisions at Tevatron [Ibid].*

Figure 4.7: Fraction of b->e to total c->e + b->e as a function of electron p_T for pp collisions at $\sqrt{s}$ = 200 GeV compared to FONLL [24].

At low and intermediate p_T, the non-perturbative correction is experimentally observed to be very small, $\mathcal{O}(\Lambda/m)$. This corrections however increases rapidly at very large p_T. A comparison between beauty differential cross section data from a $p\bar{p}$ collision at Tevatron and the non-perturbative correction prediction is shown in *Figure 4.6*. As can be seen, there is a good agreement with experimental data. Furthermore, it is apparent that NLO predictions is sufficient in order to predict the differential cross section.

Figure 4.7 shows the beauty to electron fraction relative to the total beauty and charm to electron yield as a function of the electron p_T compared to FONLL (Fixed-Order-plus-Next-to-Leading-Log) perturbative QCD calculations. As can be seen, there is a fairly good agreement between the data and the FONLL calculations. The ratio can be substituted into the R_{AA}, yielding a nuclear modification factor for charm and beauty separately. *Figure 4.8* depicts the charm and beauty decay to leptons from pp collisions at $\sqrt{s}$ = 2.76 TeV. The separation of electrons emerging from either charm or beauty provide essential information to energy loss models.
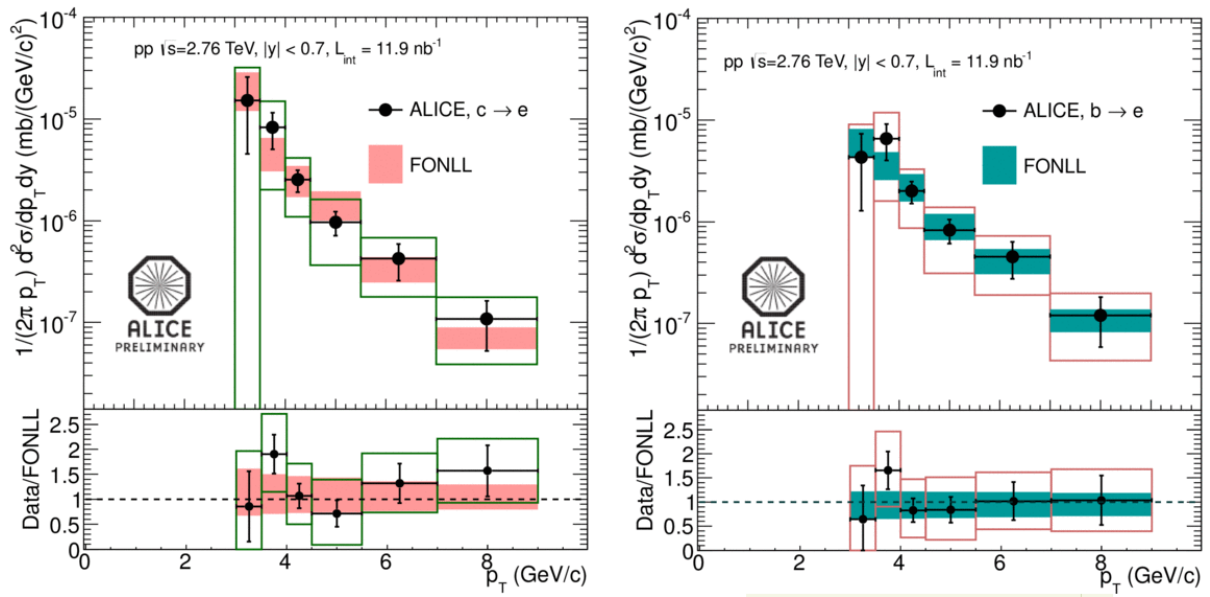
Figure 4.8: Charm (left) and beauty (right) to electron cross section as function of the electron p_T from pp collisions at $\sqrt{s}$ = 2.76 TeV [25].

Chapter 5

PYTHIA

PYTHIA is a high-energy collision event generator encompassing assorted physical models depicting the evolution of particles and the corresponding interactions [26]. PYTHIA incorporates a vast repository of hard scattering processes, several parton shower models, particle decays and various interactions. The physics covered by PYTHIA originates from theoretical models as well as parameterized empirical models determined from data fits. Since PYTHIA covers tasks such as theoretical implementations, experimental interpretations and detector performance tests, it covers the entire cycle of an experiment.

PYTHIA focuses on high-energy events, where the collisions have centre-of-mass energies $E_{CoM} > 10\ GeV$. This boundary arises from the hadron-hadron cross section approximations given by PYTHIA, which breaks down below $10\ GeV$ due to hadronic resonances not covered by any PYTHIA implementations. As of today, PYTHIA does not cover any hadron-lepton events, neither incoming photon beam collisions. The generated particles produced in the events are produced in vacuum, and PYTHIA does not include any models for the interaction with any detector elements.

5.1 PYTHIA Physics Overview

In order to describe a typical high-energy collision, an event generator should be able to accumulate several physics topics in the simulation. Simplified [27], one can characterize the evolution of an event and the corresponding physics topics as

1) Two initial particle beams approach each other with corresponding parton distributions
2) Partons from each beam branches, i.e. $q \rightarrow qg$, building up initial-state showers
3) A parton originating from each beam enter the hard scattering process, producing outgoing partons
4) The hard process might create gauge bosons which decays to partons
5) The outgoing partons branches, much like the incoming, building up final-state parton showers
6) Alongside the hard processes, partons of two incoming hadrons can also interact
7) Color confinement in hard scattering processes ensures that the quarks and gluons fragments to color neutral hadrons
8) Several produced hadrons are unstable and decay again

5.2 Hard Processes and Parton Showers in PYTHIA

PYTHIA currently contains roughly 300 various hard scattering interactions, and is optimized for $2 \rightarrow 1$ and $2 \rightarrow 2$ processes. Some of the major physics groups can be characterized by;

- *Hard QCD processes*, such as $qg \rightarrow qg$
- *Soft QCD processes*, such as inelastic scattering and minimum bias events
- *Production of heavy flavors*
- *Prompt-photon production*, such as $qg \rightarrow q\gamma$
- *Deep inelastic scattering*, such as $ql \rightarrow ql$
- *Higgs production*
- *Leptoquarks*
- *SUSY*

The cross section for some process $ij \rightarrow k$ can be written as

$$\sigma_{ij \rightarrow k} = \int dx_1 \int dx_2 \, f_i^1(x_1) f_j^2(x_2) \hat{\sigma}_{ij \rightarrow k} \, , \tag{5.1}$$

where $\hat{\sigma}_{ij \rightarrow k}$ is the hard partonic cross section and $f_i^a(x)$ are the parton-distribution functions. Due to the current lack of understanding regarding QCD, it is as of today not possible to derive hadronic parton distributions from first principles. Parameterizations based on experimental data at some momentum scale Q^2 is therefore vital in order to define parton distributions.

Either initial or final state processes containing color could yield a large gluon bremsstrahlung correction to the event topology. As the energy increases, these corrections also start contributing more to the fragmentations. There are currently two ways of dealing with these perturbative corrections. The first is the matrix-element method, where Feynman diagrams are computed from lowest to highest possible order. This would be the ideal solution as it incorporates the necessary kinematics, but the calculations become difficult at higher orders. The other approach is known as the parton-shower approach. In this case, an arbitrary number of branchings is chosen, giving a depiction of multi-jets with no clear upper limit regarding the number of embroiled partons. Due to the simplicity of the parton-shower approach, it is used more often than the matrix-element method, but the latter however is used in coupling calculations, angular distributions and other more specialized fields of studies.

5.3 Hadronization in PYTHIA

Hadronization is a QCD process where color charged partons are converted into color neutral hadrons in the presence of the confinement principle. However, since the fragmentation process has as of today yet not been derived from first principles, PYTHIA makes use of different models in order to describe the fragmentations. The three main categories are known as string fragmentation, independent fragmentation and cluster fragmentation. Although these are the main contributing models, there also exist slight variations of these as well as hybrid models. Since some of these fragmentation models

are better at certain areas of interest, the model which yields a good experimental match is usually chosen for the specific field of study when generating events.

The theoretical background for the string fragmentation model is based on the Lund model. The model itself is iterative, implying that the hadronization can be depicted as a sum of underlying branches, such as $jet \rightarrow hadron + remainder - jet$, $string \rightarrow hadron + remainder - string$ etc. For each underlying branching, the energy distributions, flavor creation and so on of the end product is based on statistics.

The main foundation of the string model is based on linear confinement of a color-singlet $q\bar{q}$ jet. Linear confinement implies a linear increase in the energy within the color field between a $q\bar{q}$ pair as the distance increases. In order to keep Lorentz covariance, the energy flow can be described using the kinetics of a massless, one-dimensional string. As the distance between the quark pairs increases, the potential energy in the string also increases to the point where it breaks and produces a new $q\bar{q}$ pair. According to the Lund model, this string breaking occurs again if the invariant mass of the string pieces is sufficiently large. In order to utilize this string fragmentation, the Lund model resort to quantum tunneling. It should be noted that this tunneling entail a suppression of heavy quarks as $u\!:\!d\!:\!c \sim 1\!:\!1\!:\!10^{-12}$.

If there are several partons present with the same origin, the string interpretation becomes a lot more complicated. For instance, in a $q\bar{q}g$ event the string span from the q to the $\bar{q}$ end via a gluon kink along the string. The hadronization of the $q\bar{q}g$ will occur along the string length, implying there is one fragmentation string between both the qg and the $\bar{q}g$. Events containing even more partons, such as $q\bar{q}gg$, invokes approximations of the matrix elements extracted from perturbation theory due to a non-well-defined color flow.

5.4 Monte Carlo in PYTHIA

Due to the nature of quantum mechanics, a means of randomness must be implemented in the event generators. This randomness is simulated by utilizing Monte Carlo methods in order to simulate probability distributions. The baseline of this randomness originates from a random number generator which yields a function capable of returning some number in a given range such that a distribution depicts a flat line in the given range.

One of the most common situations involves a real function $f(x)$ defined in some range $x \in [x_{min}, x_{max}]$ where one desires to choose a random x such that in an infinitesimal range dx close to x, some probability of interest is proportional to $f(x)dx$. The function $f(x)$ can be a cross section, a means of describing hadronization or other distributions.

One of the intriguing features offered by Monte Carlo methods is the fact that choosing some specific well-defined value of x yields a normalized result. Integration over $f(x)$ can also sometimes contain information on an overall sum as well as specific constituents, such as the case where x represents phase-space and $f(x)$ denotes some differential cross section. In this case, integration is a means of obtaining the total cross

section. This means Monte Carlo simulations can generate events step-wise as well as approximate the total cross section.

5.5 Particle Codes

The Particle Data Group numbering scheme is used for particle identification, where each particle is assigned a specific KF particle code corresponding to the PDG standard [28]. Table 5.1 depicts an excerpt of some KF codes for quarks and leptons. The anti-particles, assuming they exist, are defined by the negative KF code of the corresponding particle.

Table 5.1: Quark and lepton KF codes

KF	Name	KF	Name
1	d	11	e^-
2	u	12	ν_e
3	s	13	μ^-
4	c	14	ν_μ
5	b	15	τ^-
6	t	16	ν_τ
7	b$'$	17	τ'
8	t$'$	18	ν'_τ

5.6 The Event Record

The information regarding produced particles is stored in the event record. The event record contains information about flavors, charge, momentum, energy and vertices. The generated events are stocked in "storage blocks" known as PYJETS. In these blocks, each generated particle occupy a line in a matrix. The various matrix constituents corresponding to this line yield information on what kind of particle it is, the origin of the particle, current state, momentum, mass and the production vertex. As of today, a PYJETS block can contain 4000 entries.

5.7 Parton Distributions

The parton distribution function $f_i^a(x, Q^2)$ depicts the probability of finding a specific parton i with fractional beam energy x where the particle a is exposed to a hard scattering at some scale Q^2. In the case of protons, there exist many distribution sets obtained from experimental data where the Q^2 dependence is in conformity with QCD equations. The default in PYTHIA is the leading-order set CTEQ 5L, although there are several other sets

available of choice. Meson parton distributions however are rare, and the only sets available are for the $\pi^{\pm}$.

5.8 Cross Sections in PYTHIA

In the $1 + 2 \rightarrow 3 + 4$ event generation, PYTHIA makes use of the variables

$$\hat{s} = x_1 x_2 s \tag{5.2}$$

$$\tau \equiv x_1 x_2 = \frac{\hat{s}}{s} \tag{5.3}$$

$$y = \frac{1}{2} \ln \frac{x_1}{x_2} \tag{5.4}$$

$$z = \cos \hat{\theta} \tag{5.5}$$

$$\beta_{34} = \left\{ \left(1 - \frac{m_3^2}{\hat{s}} - \frac{m_4^2}{\hat{s}} \right)^2 - 4 \frac{m_3^2}{\hat{s}} \frac{m_4^2}{\hat{s}} \right\}^{1/2} \tag{5.6}$$

$$\hat{t} = -\frac{\hat{s}}{2} \left(1 - \cos\hat{\theta} \right), \tag{5.7}$$

where s is the total squared centre-of-mass energy, m_3 and m_4 are the masses of the outgoing particles and $\hat{\theta}$ is the polar angle of the 3rd parton in the centre-of-mass frame. The cross section for the process $1 + 2 \rightarrow 3 + 4$ can be written as

$$\sigma = \iiint \frac{d\tau}{\tau} dy \, d\hat{t} x_1 f_1(x_1, Q^2) x_2 f_2(x_2, Q^2) \frac{d\hat{\sigma}}{d\hat{t}}, \tag{5.8}$$

where $d\hat{\sigma}/d\hat{t}$ denotes the differential cross section. However, in order to achieve an equitable efficiency regarding Monte Carlo, kinematic peaks should ideally be depicted by separate terms to avoid fluctuations. By introducing the distributions $h_\tau(\tau), h_y(y)$ and $h_z(z)$ according to the variables can be generated separately. For τ, the allowed span is given by $\tau \in [\tau_{min}, \tau_{max}]$ which is predefined by the user. Mass cuts for instance directly restricts τ. For y the range is constrained by $|y| \leq -1/2 \ln \tau$ and other user-defined boundaries, and z is usually defined in the range $z \in [-1, 1]$. One should however note that some cross sections diverge as $z \rightarrow \pm 1$, implying a need of regularization.

After an initial choice for the variables, the cross section can be written as

$$\sigma = \langle \frac{\pi}{s} \frac{\beta_{34}}{\tau^2 h_\tau(\tau) h_y(y) 2 h_z(z)} x_1 f_1(x_1, Q^2) x_2 f_2(x_2, Q^2) \frac{\hat{s}^2}{\pi} \frac{d\hat{\sigma}}{d\hat{t}} \rangle. \tag{5.9}$$

It is obvious that the cross section for the Monte Carlo generated event can be interpreted as a product of four terms;

1) The factor π/s which yields the dimension of the cross section in units of GeV^{-2}.
2) The second term describes the Jacobian, atoning any changes in phase-space.
3) The parton distribution functions obtained from the available libraries in PYTHIA
4) The term $(\hat{s}^2/\pi) \, d\hat{\sigma}/d\hat{t}$, a dimensionless number which has to be manually coded depending on the process depicting the actual physics content.

In PYTHIA, the cross section is determined as the average over all generated phase-space. The total hadronic cross section σ_{tot}^{AB} for $A + B \rightarrow anything$ is determined using a parameterization. This method involves writing the cross section as

$$\sigma_{tot}^{AB}(s) = X^{AB} s^\epsilon + Y^{AB} s^{-\eta} \, , \tag{5.10}$$

where $s = E_{CoM}^2, \epsilon = 0.081$ and $\eta = 0.453$. The coefficients X^{AB} and Y^{AB} are specified by the initial state.

5.9 Particle Decays

Initiating a decay in PYTHIA involves one or two present resonances, for instance $q\hat{q}' \rightarrow W^+$ or $qg \rightarrow W^+ q'$. The decay channel of the corresponding resonance is chosen based on relative weights assessed at the resonance mass. The angular distribution of the decay resonances are selected in the corresponding rest frame, and can be user specified if needed. Based on these angular distributions, PYTHIA constructs the four-momenta of the decay particles in the correct reference frame. At this point, PYTHIA evaluates the various matrix elements and adds constraints based on underlying cross sections. If the angles fall in an acceptable range, PYTHIA includes fermion masses and allows quarks and leptons to radiate. Restrictions of decay channels are already implemented in the hard-scattering cross sections, which greatly simplifies mixing of different events.

5.10 Quark Flavors in PYTHIA

PYTHIA enables the selection of various production sub-processes by letting the user combine and choose events according to a numbering scheme known as ISUB codes. For instance, some events and their corresponding ISUB codes are

11     $q_i q_j \rightarrow q_i q_j$

12     $q_i \bar{q}_i \rightarrow q_j \bar{q}_j$

13     $q_i \bar{q}_i \rightarrow gg$

28     $q_i g \rightarrow q_i g$

53     $gg \rightarrow q_i \bar{q}_i$

68     $gg \rightarrow gg$

All these topologies are $2 \rightarrow 2$ events with cross sections proportional to α_s^2. The corresponding Matrix elements and Feynman amplitudes are for mass-less quarks, implying divergent cross sections as the $p_\perp \rightarrow 0$, thus enforcing regularization.

All new produced flavor, referring to the annihilation processes given by ISUB 12 and 53, are delineated by the conservation of flavor regarding gluon splitting processes. For the production of heavy flavors, the dominant QCD production processes are

81      $q_i \bar{q}_i \rightarrow Q_j \bar{Q}_j$

82      $gg \rightarrow Q_j \bar{Q}_j$

Heavy flavors can also be present in parton distributions of hard scatterings at the corresponding Q^2 scale. Examples are flavor excitation and gluon splittings during the evolution of the parton shower. These processes start contributing as the centre-of-mass energy increases. For instance, at LHC energies only ~15% of the production of beauty quarks are due to lowest-order topologies.

For Monte Carlo studies of charm and beauty production, it can be of interest to simulate the full evolution of some experiment and only keep the events containing charm or beauty originating from either flavor creation, excitation or gluon splitting. Referring to ISUB 12 and 53, note that the production of charm and beauty is equivalent to ISUB 81 and 82. The conversion from ISUB 12 to 81 is pretty straight forward since the exchange of s-channel gluons is the only contribution. In the case of ISUB 53 however, a new evaluation of the matrix elements of charm and beauty is required. This is done by keeping both the $\hat{s}$ and $\hat{\theta}$ values already user-defined and adjust $\hat{t}$ with the massive masses.

As previously mentioned, PYTHIA utilizes an iterative method to describe hadronization. By default, PYTHIA gives an initial quark q_0 such that a newly created $q_1 \bar{q}_1$ pair form a meson as $q_0 \bar{q}_1$, whereas the remaining q_1 is left behind to pair with another quark. In order to produce the various mesons, the relative probabilities for the production of the various $q\bar{q}$ pairs is needed. In order to generate $q\bar{q}$ pairs, PYTHIA uses the Lund model to predict the probability of a quantum tunneling effect where the quarks are created at some specific point and then tunnel out in a valid, classic region. As a function of the common transverse mass m_T, the quantum tunneling probability is given by

$$\exp\left(-\frac{\pi m_T^2}{\kappa}\right) = \exp\left(-\frac{\pi m^2}{\kappa}\right)\exp\left(-\frac{\pi p_T^2}{\kappa}\right), \tag{5.11}$$

where we have introduced the string tension constant $\kappa \sim 1 GeV/fm$. By introducing this factorization it is possible to create independent momentum component spectrums for the created quark pairs.

5.10.1 Fragmentation Functions in PYTHIA

Assuming a $q\bar{q}$ jet where the q moves along the $+z$ direction and the $\bar{q}$ along $-z$, it can be shown that the momentum component distributions indicate a Gaussian distribution. PYTHIA regulates these momentum distributions by a single parameter, yielding the root-mean square p_T of the quarks. The hadron p_T is then constructed as the sum of the transverse momentum of the quarks. In order to determine the energy and the longitudinal momentum of the created hadron, PYTHIA is forced to only use one variable since the hadron momentum is restrained by the transverse mass of the hadron. This

leads to the option of defining z as a fraction of the sum of the energy and p_z carried by the hadron.

The probability of choosing a given z is given by the fragmentation function $f(z)$. However, the choice of $f(z)$ is selected by PYTHIA. For instance, if one requires a fragmentation in which the fragmentation process is symmetric, the fragmentation function is given by

$$f(z) \propto \frac{1}{z} z^{a_\alpha} \left(\frac{1-z}{z}\right)^{a_\beta} \exp\left(-\frac{bm_T^2}{z}\right), \tag{5.12}$$

where the parameter a is a factor denoting flavor, α corresponds to the previous flavor in the iteration procedure and β is the new flavor. The parameter b is defined by PYTHIA. There are other fragmentation functions available as well, such as the Field-Feynman parameterization given by

$$f(z) = 1 - a + 3a(1-z)^2, \tag{5.13}$$

where a this time is given by $a = 0.77$. This fragmentation function is primordially used for hadrons consisting of either up, down or strange quarks. In the case of heavy flavors such as charm and beauty, the best representation is given by the Peterson formula

$$f(z) \propto \frac{1}{z\left(1 - \frac{1}{z} - \frac{\epsilon}{1-z}\right)^2}, \tag{5.14}$$

where $\epsilon \propto 1/m_Q^2$.

5.11 Data Analysis

In Monte Carlo simulations, one is able to study particles on two levels known as the kinematic level and the reconstruction level. The kinematic level is where the particles are generated by event generators as discussed in Chapter 3.1.1. The reconstruction level depicts the particle propagation through the detectors. The analysis in this thesis is based on two Monte Carlo simulations, LHC10f6a and LHC10f7a. Both runs are PYTHIA generated proton-proton events at $\sqrt{s} = 7\ TeV$. The run LHC10f6a is a minimum bias run, with $\approx 172 \times 10^6$ events. The run LHC10f7a is an enhanced sample regarding charm and beauty flavors with $\approx 31 \times 10^6$ events.

Figure 5.1 and *5.*2 depicts the rapidity distribution for generated charm and beauty quarks for the two data sets normalized to the simulated number of events N. Comparing the two distributions, it is apparent that the enhanced sample show a more defined peak at $y{\sim}0$. For the analysis task, a rapidity cut given by $|y| < 1$ is applied in order to focus the analysis on mid-rapidity physics.

The transverse momentum distribution p_T for charm and beauty quarks from the enhanced sample and the minimum bias run are given in *Figure 5.3 – 5.4*. The two distributions are very similar in shape, the only major difference that can be witnessed is the difference in the number of statistics.
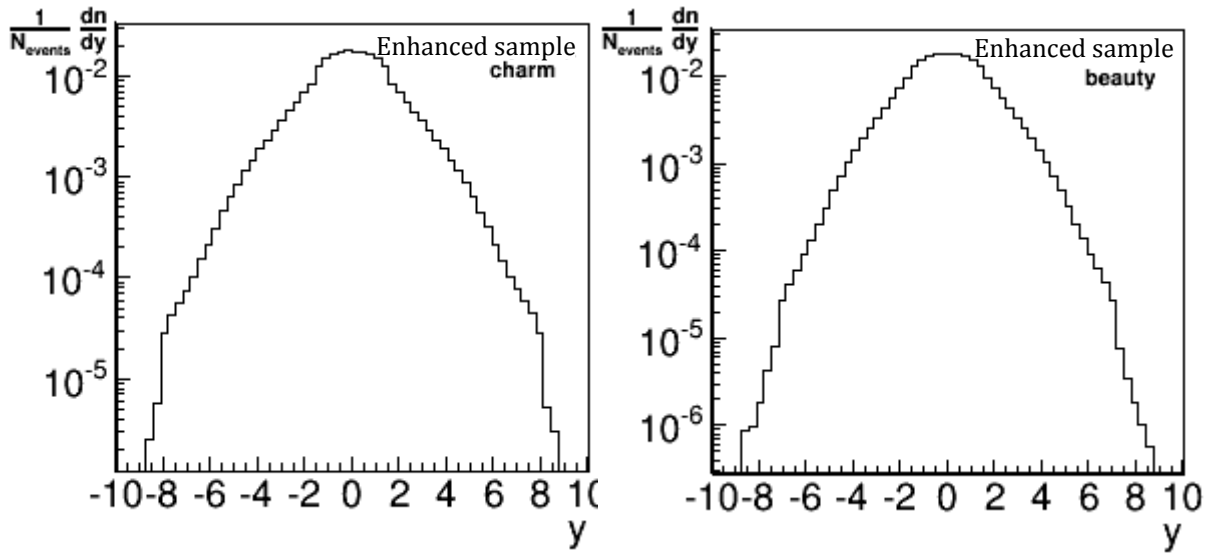
Figure 5.1: Rapidity distributions for charm and beauty quarks from the enhanced PYTHIA sample.
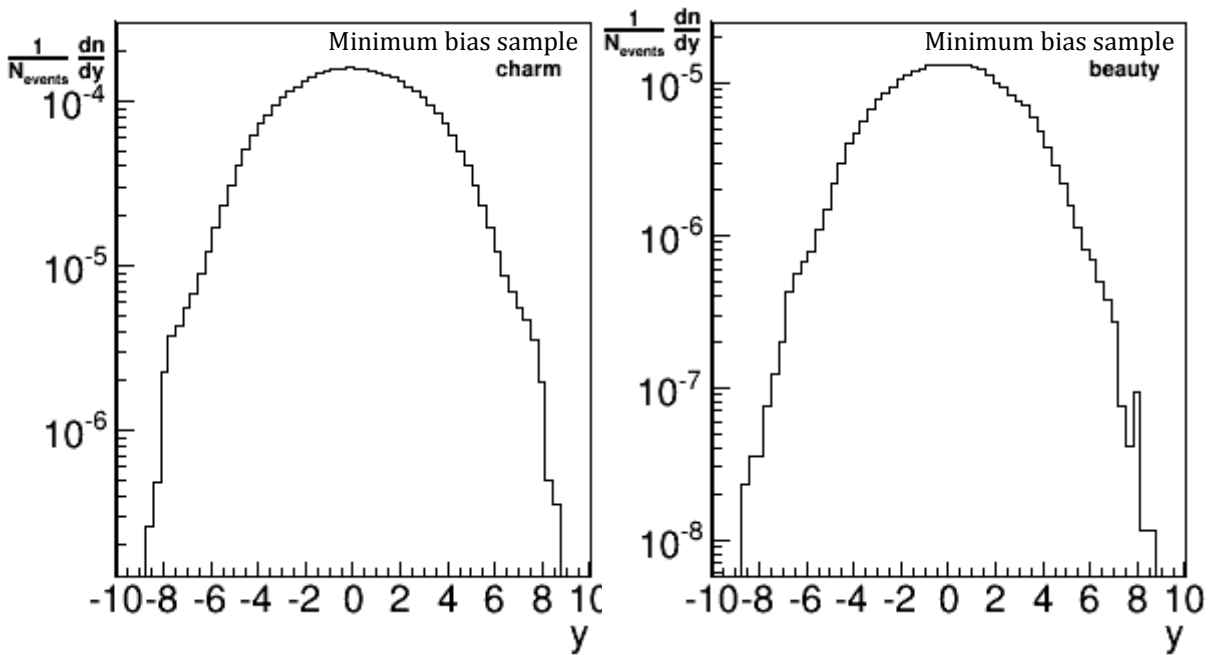

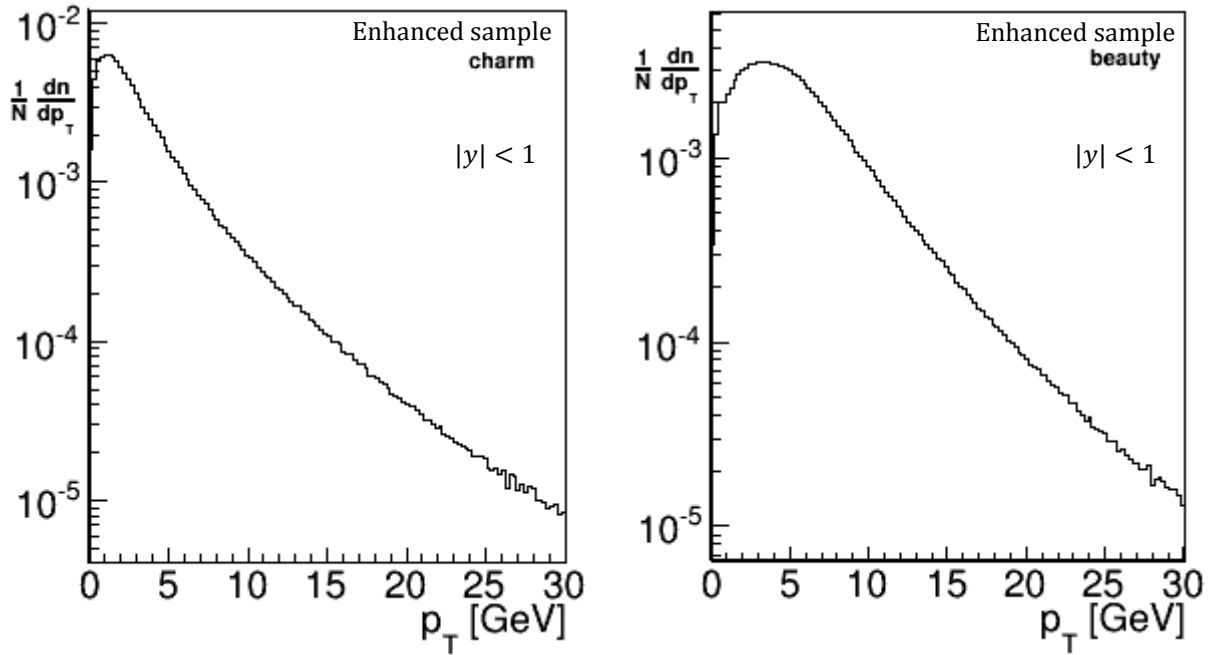*Figure 5.2: Rapidity distributions for charm and beauty quarks from the minimum bias sample.*

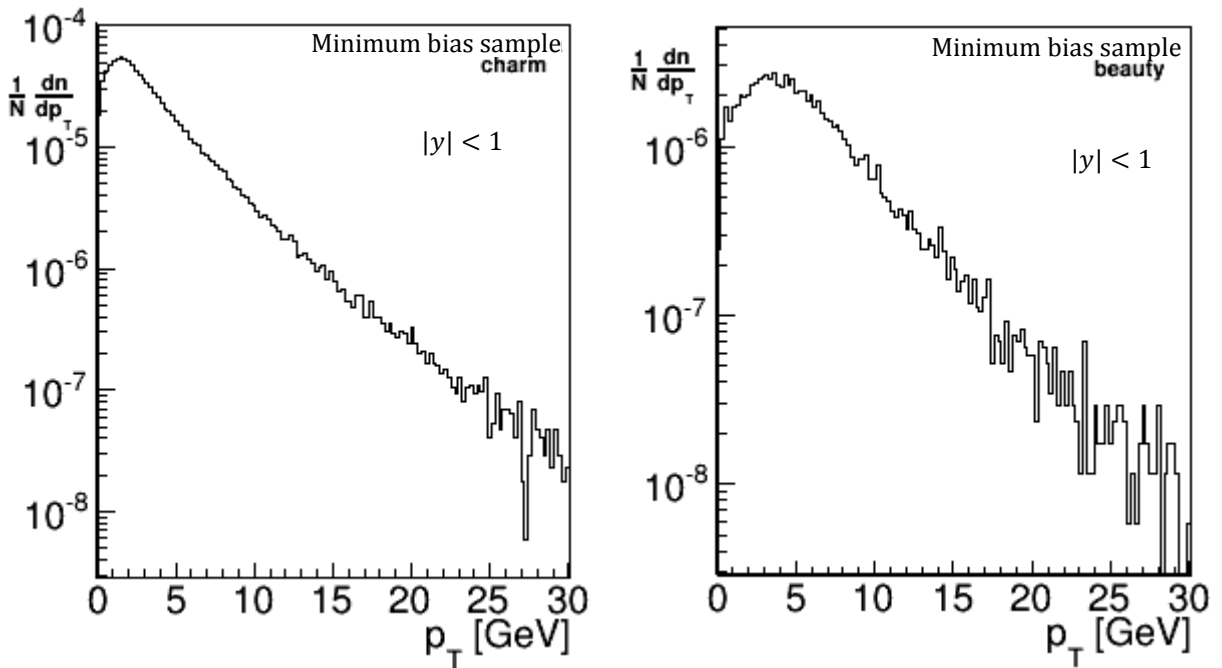*Figure 5.3: Transverse momentum distribution of charm and beauty quarks from the enhanced sample.*

Figure 5.4: Transverse momentum distribution of charm and beauty quarks from the minimum bias sample.
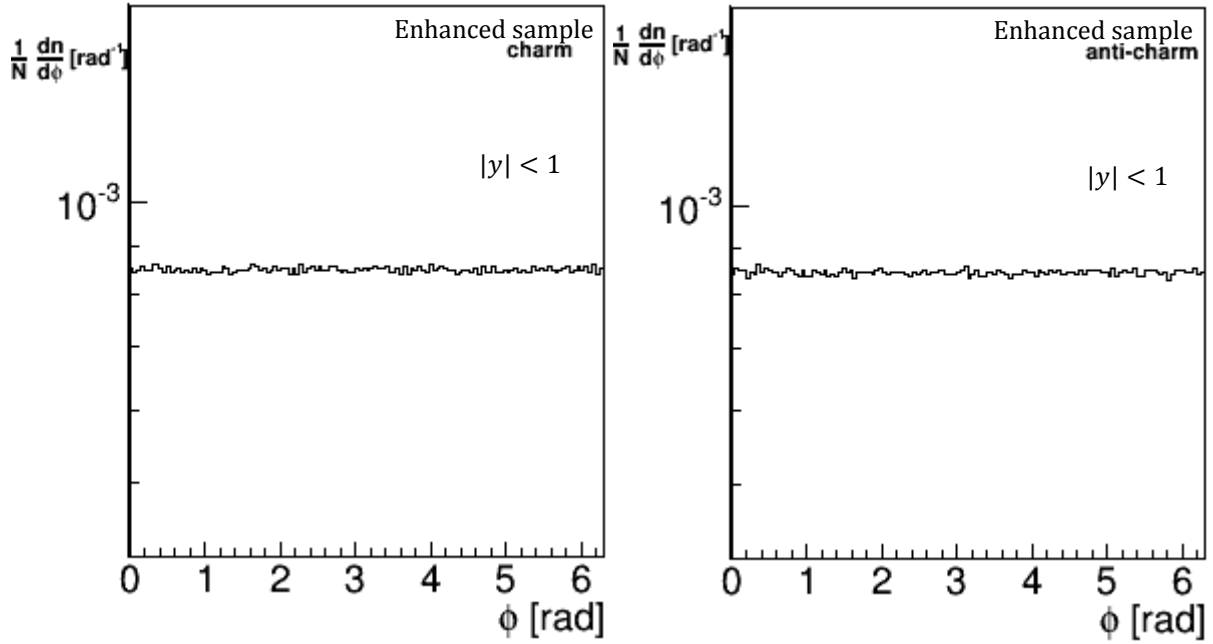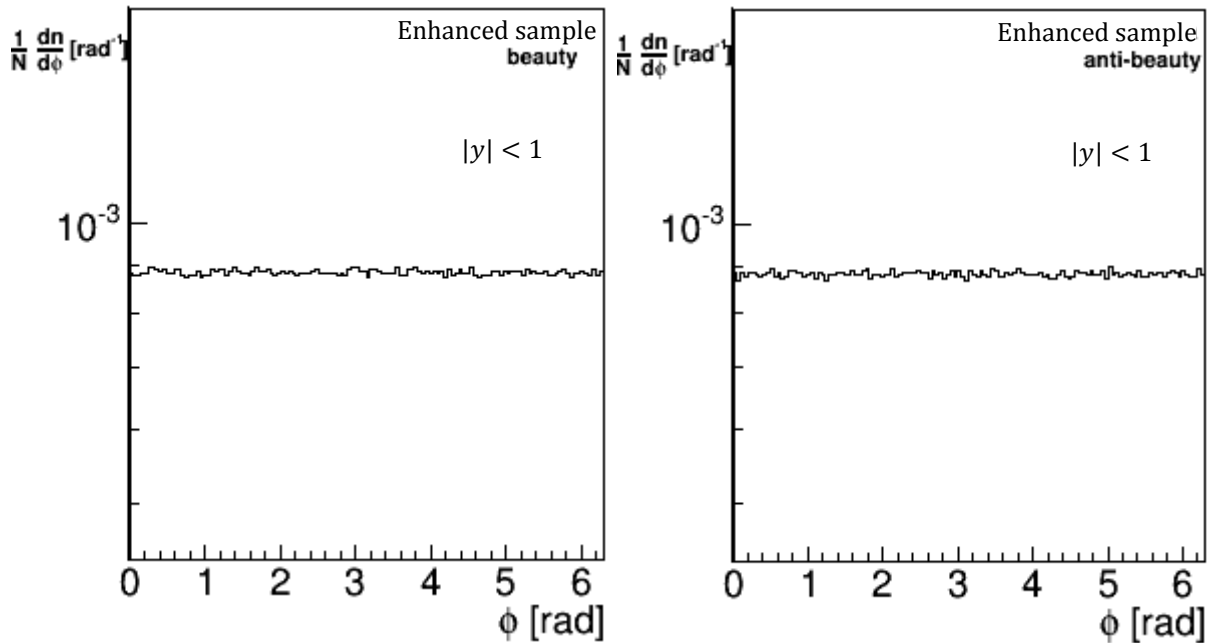
Figure 5.5: The azimuthal distribution of charm and anti-charm quarks from the enhanced sample.

Figure 5.6: The azimuthal distribution of beauty and anti-beauty quarks from the enhanced sample.
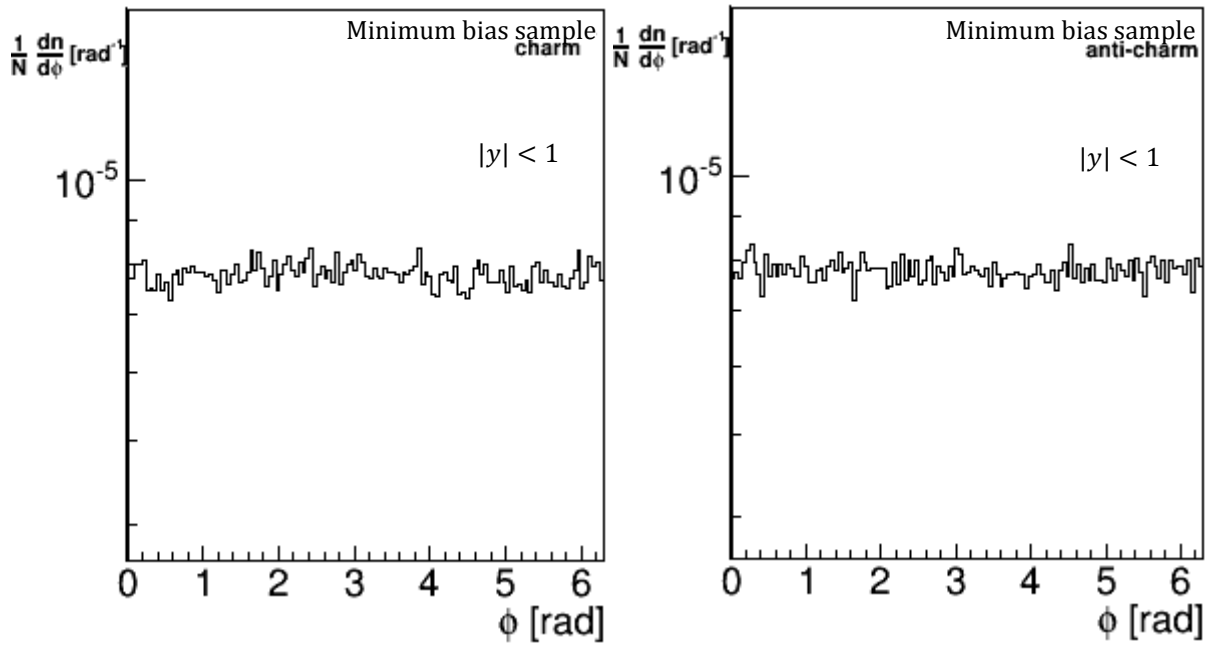
Figure 5.7: The azimuthal distribution of charm and anti-charm quarks from the minimum bias sample.
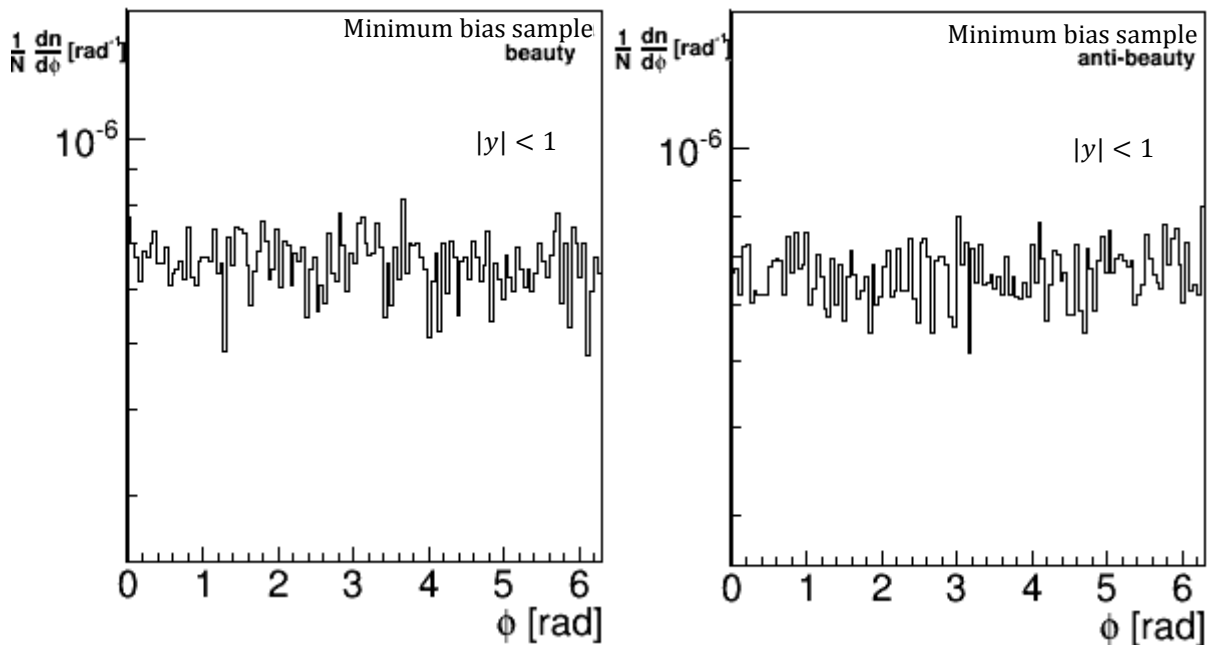
Figure 5.8: The azimuthal distribution of beauty and anti-beauty quarks from the minimum bias sample.

Figures 5.5 – 5.8 depicts the azimuthal distributions for charm and beauty quarks as well as the azimuthal distributions of the corresponding anti-particles. As expected, all quarks are pretty much evenly distributed in the φ space. The study of azimuthal correlations will be elaborated in greater detail in the following chapter.

The rapidity distributions of electrons originating from heavy flavor particles is given in *Figure 5.9*. Comparing the two samples clearly show that the distributions deviate from each other, a feature which also is witnessed when comparing the rapidity distributions of D^0 mesons for the two samples as seen in *Figure 5.10*. In both cases, the enhanced sample show a more pronounced peak as $y \rightarrow 0$. The transverse momentum distribution of both heavy flavor electrons and D^0 mesons can be seen in *Figures 5.11 – 5.12.*
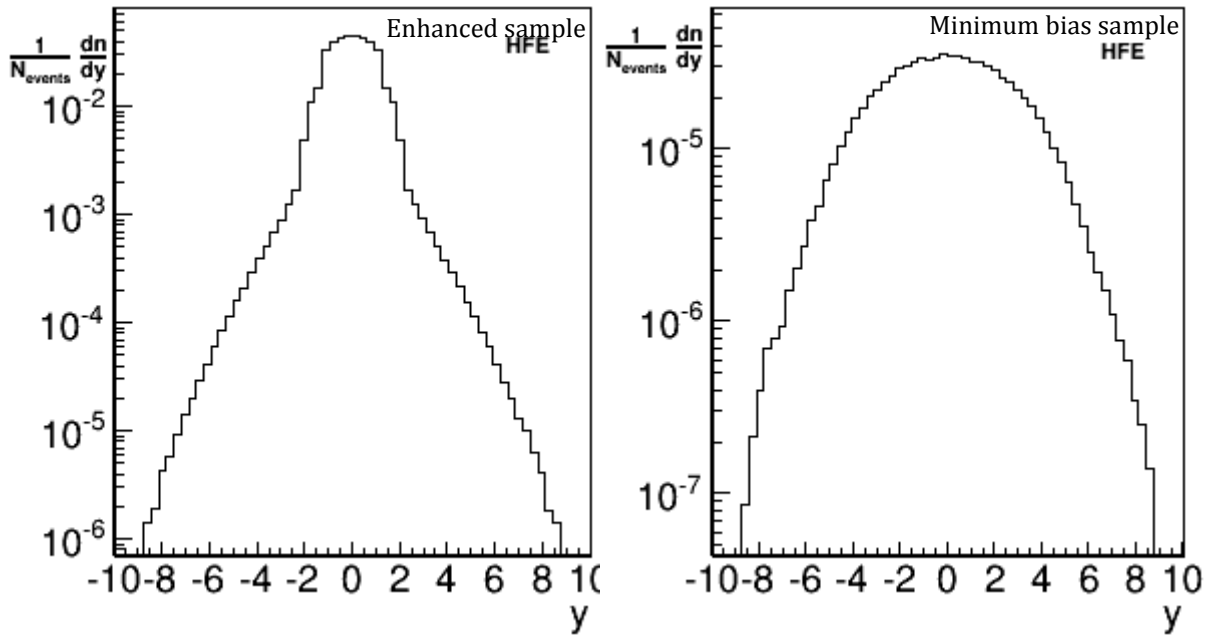
Figure 5.9: The rapidity distributions of heavy flavored electrons obtained from both the enhanced sample and the minimum bias sample.
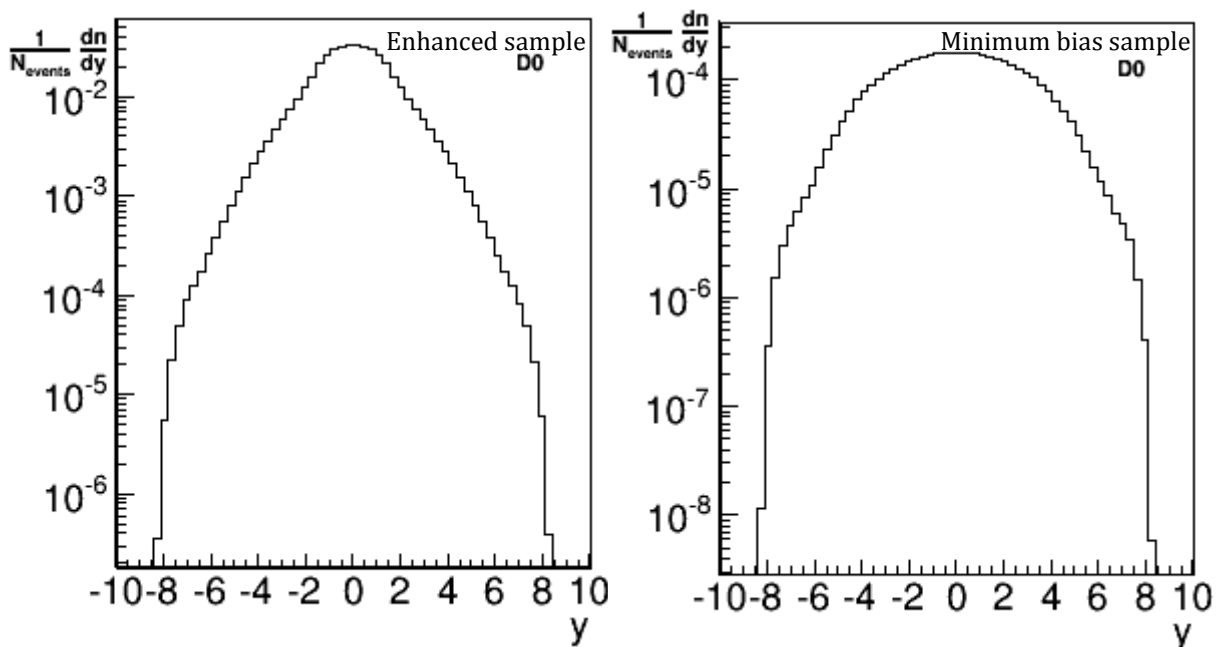
Figure 5.10: The rapidity distributions of D^0 mesons obtained from both the enhanced sample and the minimum bias sample.
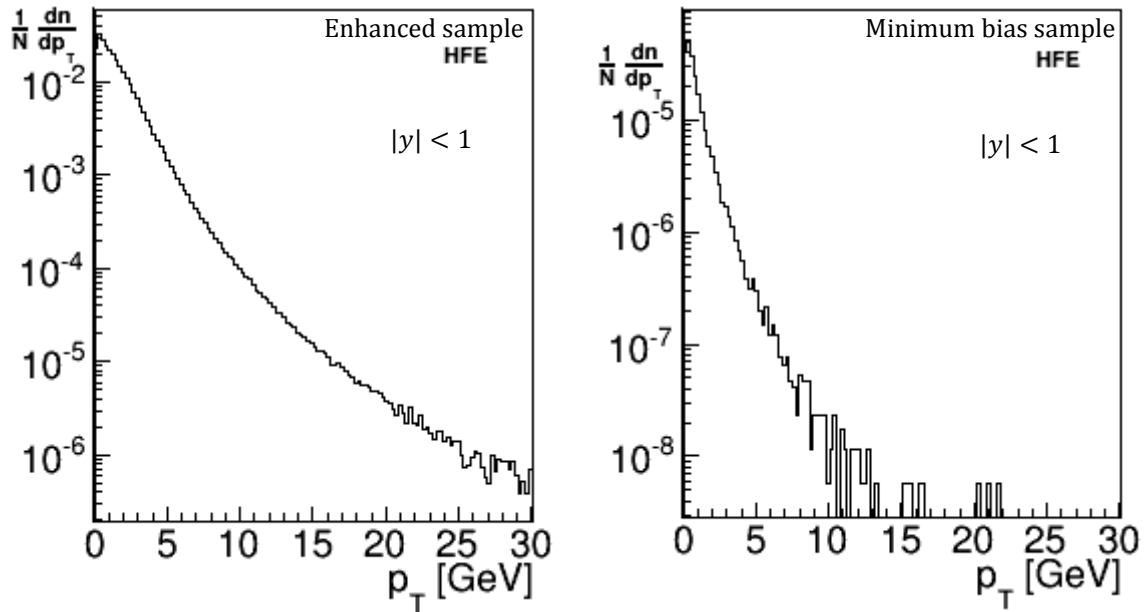
Figure 5.11: The p_T distribution of heavy flavored electrons obtained from both the enhanced sample as well as the minimum bias sample.
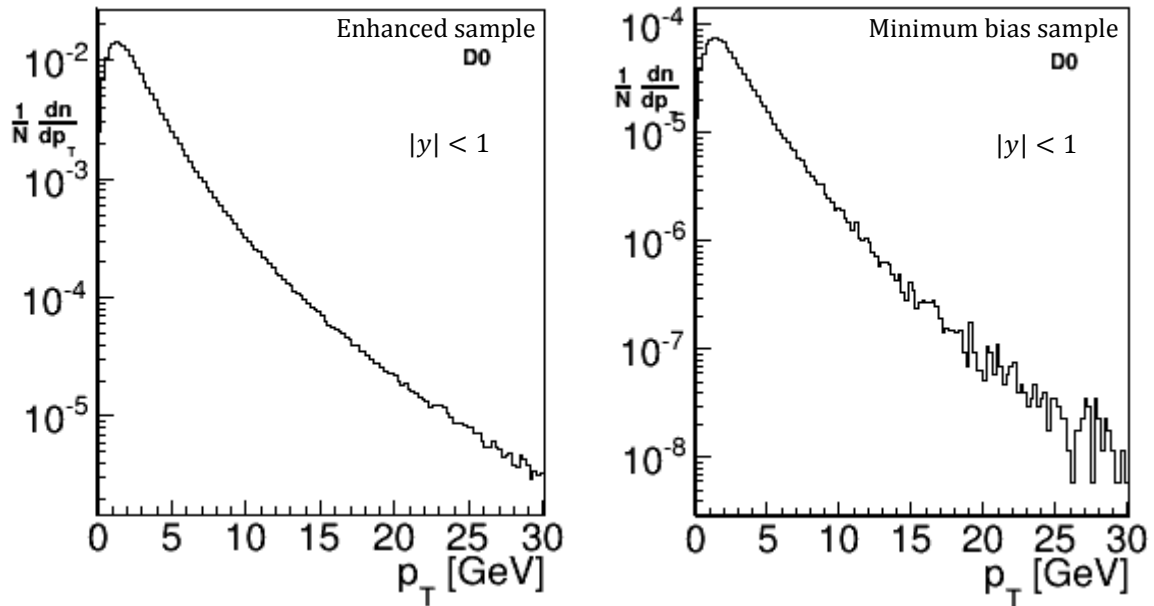

Figure 5.12: The p_T distribution of neutral D mesons obtained from the enhanced sample and the minimum bias sample.

46

Chapter 6

Azimuthal Correlations

As briefly mentioned in Chapter 1, various properties of matter can be divulged through the study of energy loss of particles traversing it. For instance, partonic energy loss models expounding the R_{AA} convey information regarding the interaction between heavy quarks and the medium. Electrons originating from heavy flavor particles (which henceforth will be denoted HFE) is a great asset for determining energy loss mechanisms in QGP. Moreover, the separation of HFEs emerging from either beauty or charmed particles is an important attribute to energy loss models [29].

However, the R_{AA} does not yield much information regarding heavy flavor production mechanisms. Therefore, azimuthal correlations of heavy flavor particles are introduced as observables. Referring to Chapter 4.2, the produced heavy quarks fragment into particle showers in azimuth. A valid assumption is therefore the observation of two distributions, one on the near-side, i.e. $\Delta\varphi = 0$, and one on the away side, i.e. $\Delta\varphi = \pi$, when measuring the relative angle between the heavy flavored particles.

As partons traverse a QCD medium, they experience an energy loss depending on the path length, the QCD medium and the parton mass. In particular, partons lose energy due to gluon bremsstrahlung as the partons scatter inelastic from the constituents of the medium. It can be shown that this radiative energy loss can be expressed as

$$\Delta E_{rad} \propto \alpha_S L^2 \,, \tag{6.1}$$

where L is the path length in the medium. Theoretical predictions based on perturbative QCD (pQCD) suggests that heavy quarks should experience less energy loss as they traverse the QGP compared to lighter quarks due to the dead-cone effect. However, experiments reveal a suppression of high-p_T electron yields from semi-leptonic heavy flavor decays [30] to the same yield of light flavor hadrons. Distinguishing charm and beauty could contain valuable insight into the energy loss mechanisms as the corresponding contributions can be studied separately. This separation can be achieved through the study of heavy flavor azimuthal correlations.
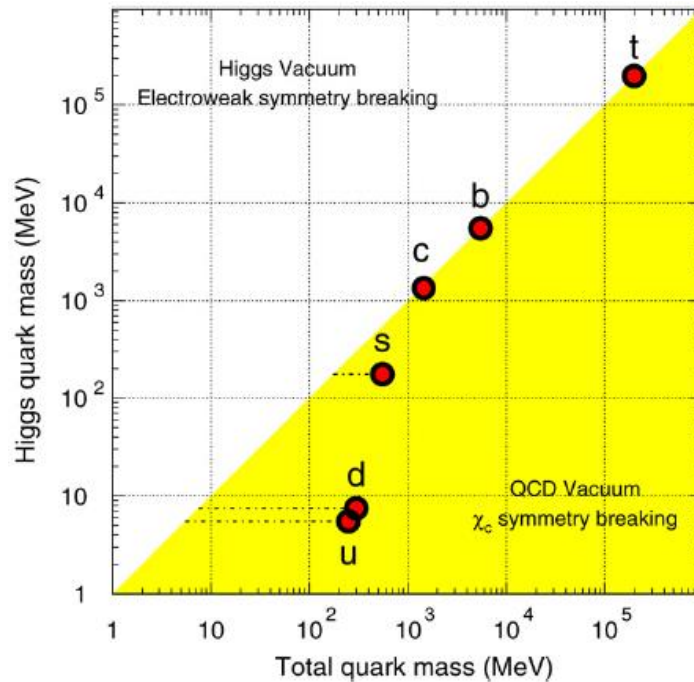
Figure 6.1: Schematic overview of the various quark masses in the Higgs vacuum [31].

6.1 Heavy Flavor Azimuthal Correlations

According to Quantum Field Theory (QFT), all "bare" quark masses outlined in the Lagrangian diverge to infinity, but divergent propagator loop contributions abrogate them, creating finite masses. For instance in the case of electrons, QFT predicts an infinite bare electron mass that's actually well-defined if the mass "runs" from infinity at small length scales to some convergent constant at large scales. In the case of quarks however, the mass diverges at some energy scale Λ_{QCD} instead of converging. This is an interesting result of QCD as it implies the meaninglessness of the concept of the mass of the quarks relative to a "macroscopic" observer since the masses diverge at way smaller scales. The latter gives rise to the principle of quark confinement and the fact that bare quarks are not observable. That being said, one can define quark masses by utilizing renormalization schemes. One can successfully convert different scales by renormalization groups, which is neatly covered by perturbation theory. Videlicet, different quark masses can all be "true" but are covered by different renormalization scales. There is however another interpretation of the quark mass known as the constituent quark, or valence quark, mass. Valence quarks can be interpreted as bare quarks enclosed within a sea of virtual gluons and quarks, i.e. they are not directly related to the mass parameters of the Lagrangian but more of a representation of chiral symmetry breaking.

The heavy flavors charm and beauty are suited probes since their large masses are engendered by dint of their coupling to the Higgs field in disparity to the light quark masses which are dominated by spontaneous chiral symmetry breaking (see *Figure 5.1*). In other words, the light quarks are rendered with the corresponding bare current masses in a QGP while the masses of the heavy flavors stay massive. Alongside the fact that the heavy flavors are produced early in the pQCD processes, the number of heavy flavor particles is in general conserved since the temperature of the QGP is smaller than the masses of charm and beauty, minimizing risks of secondary pair production mechanisms.

Figures 6.2 – 6.6 depict the azimuthal correlations for charm and beauty quarks from the enhanced and the minimum bias sample at various momentum cuts. Referring to *Figure 6.2,* with no p_T cuts applied, we clearly see the back-to-back scattering peak at $\Delta\varphi = \pi$. This is due to the LO process flavor creation as well as the NLO flavor excitation process where the particles are correlated in azimuth in order to not violate momentum conservation. In the area $\Delta\varphi = 0$, the gluon splitting process dominates. Note the difference of the charm $\Delta\phi$ distributions when comparing the enhanced and the minimum bias sample on the near-side. While the minimum bias set shows a clear and defined peak, the enhanced sample is much less pronounced. A very subtle double-peak is also apparent.

Referring to *Figure 6.3,* which depict the charm and beauty azimuthal correlations at $0 \, GeV < p_T < 1 \, GeV$, the distribution is completely dominated by a same-side orientation, implying that gluon splitting is the main contributor at this p_T range. Note also how the distributions from the two runs deviate considerably, where the enhanced sample now clearly shows a double-peak feature on the near-side compared to the minimum bias run for the charmed case. The lack of statistics regarding the minimum bias run for the beauty case makes it hard at this point to draw any conclusions however. By increasing the momentum cut to $1 \, GeV < p_T < 4 \, GeV$, referring to *Figure 6.4,* the away-side starts contributing to the distribution. This feature is apparent in both simulations, implying the presence of all heavy flavor production processes. It should be noted that in this p_T range, both simulations are in agreement in the case of the beauty $\Delta\phi$ distribution. For the charm case, both runs seem to accommodate the same away-side distribution, whilst the near-side is again dominated by a double-peak for the enhanced sample.

Increasing the momentum cut further to $4 \, GeV < p_T < 10 \, GeV$, referring to *Figure 6.5*, clearly shows how the distribution is completely dominated by back-to-back processes with a very distinct peak on the away-side. At this p_T range, both the enhanced sample and the minimum bias run seem to be in agreement.

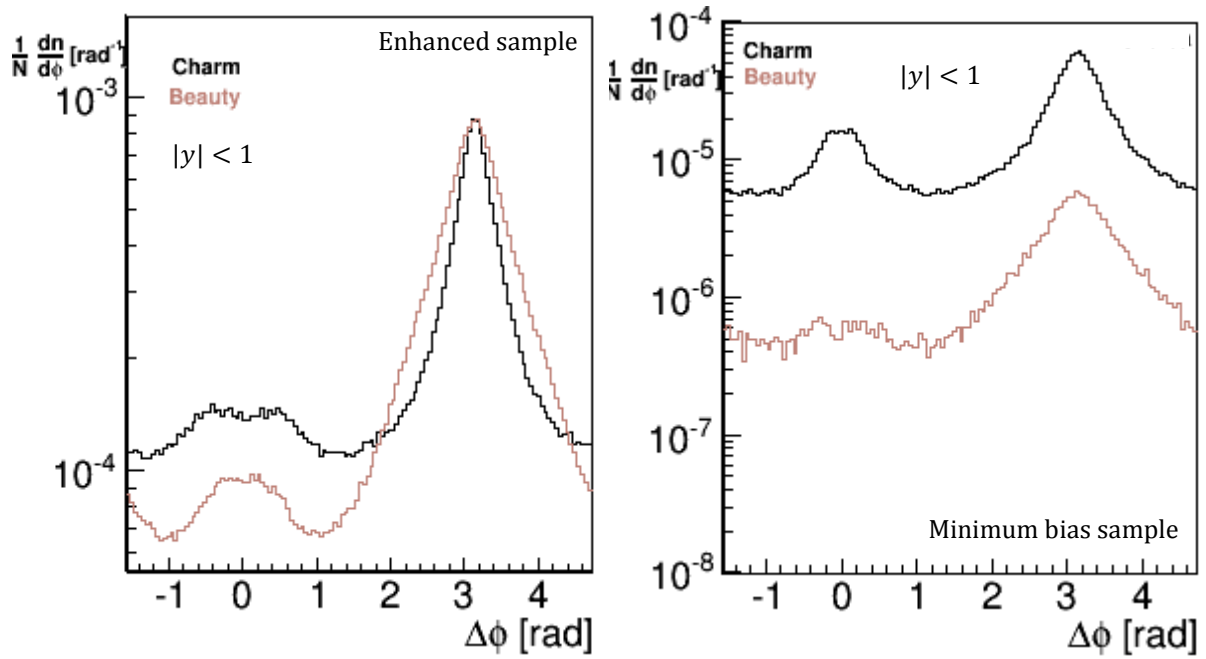*Figure 6.2: Azimuthal correlations of charm and beauty quarks from PYTHIA generated p-p collisions at √s = 7 TeV.*

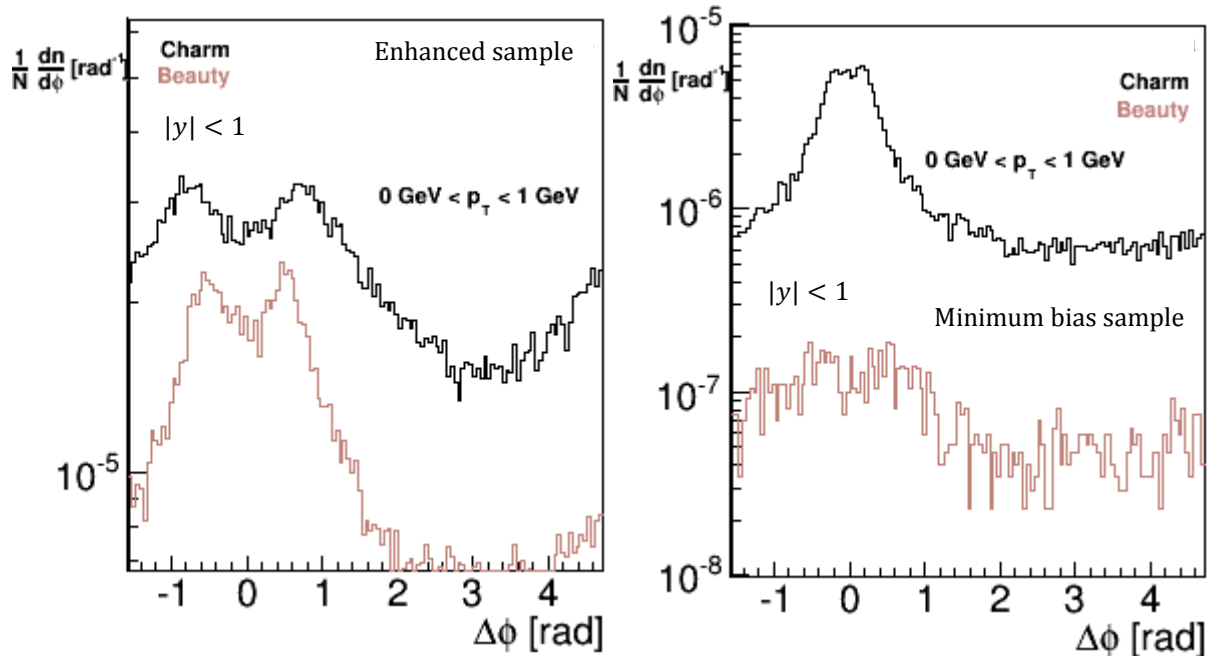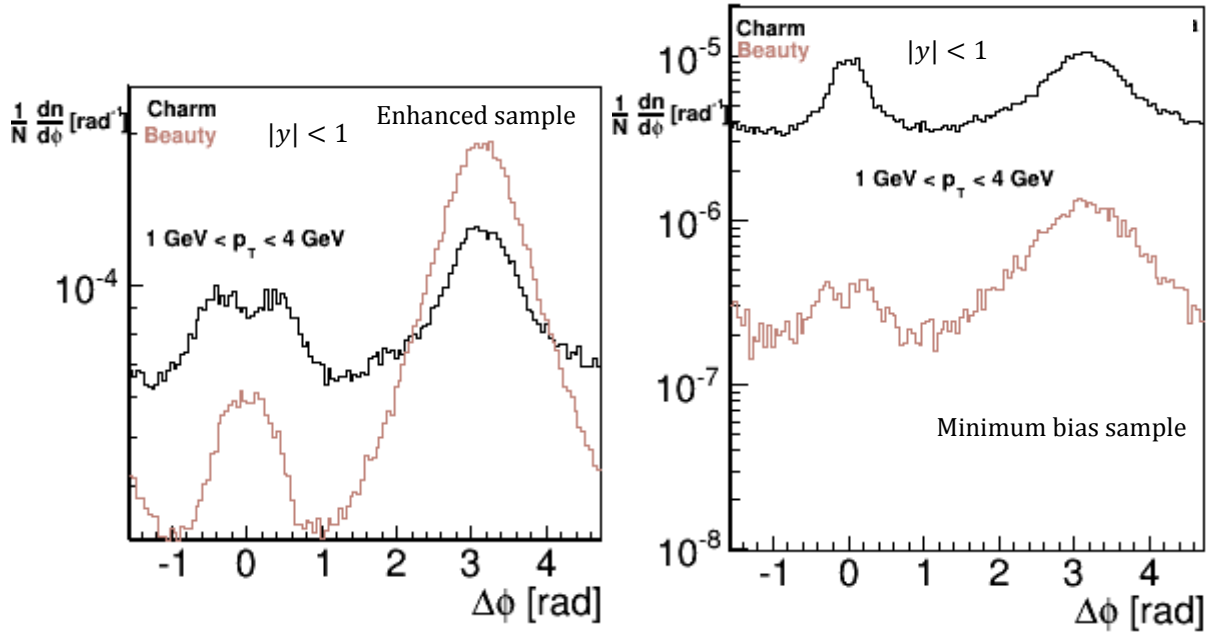*Figure 6.3: Azimuthal correlations of charm and beauty quarks from PYTHIA generated p-p collisions at √s = 7 TeV with* $0\ GeV < p_T < 1\ GeV$.

Figure 6.4: Azimuthal correlations of charm and beauty quarks from PYTHIA generated pp collisions at √s = 7 TeV with $1\ GeV < p_T < 4\ GeV$.
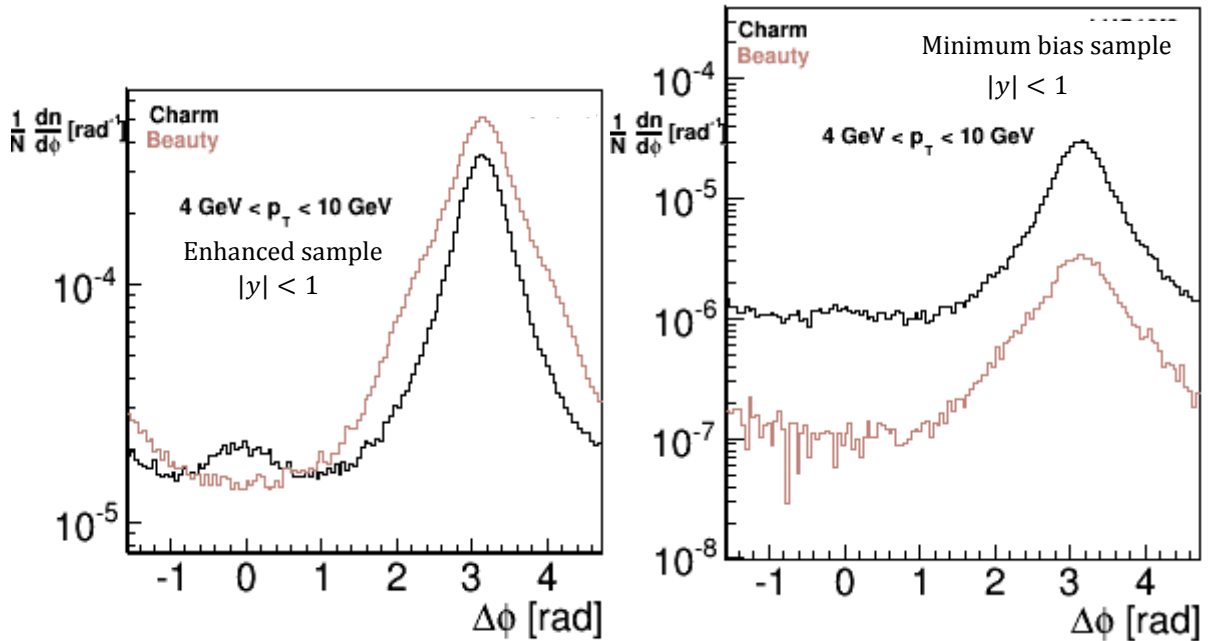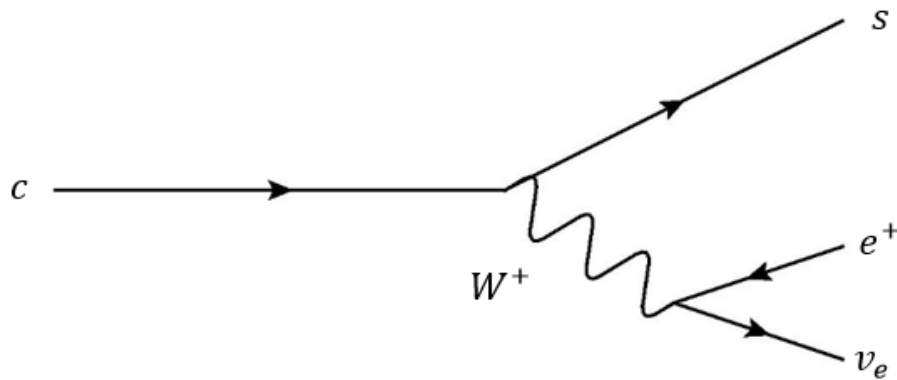

Figure 6.5: Azimuthal correlations of charm and beauty quarks from PYTHIA generated pp collisions at √s = 7 TeV with $4\ GeV < p_T < 10\ GeV$.

Figure 6.6: Feynman diagram of a typical charm decay.

6.2 The D^0 Meson

As the heavy flavors decay, there appears to be a correlation between the charge parity (CP) of the original flavor and the CP of the emerging constituents. When studying the decay channels of charmed particles, charm decays in plethora to positrons instead of electrons. The anti-charm results similarly in an abundance of electrons. In the case of beauty, the decay channels show an affluence of electrons and analogous to the charm case an abundance of positrons for anti-beauty. This however can be explained by the properties of CP. Quarks can change flavor via the electroweak interaction, i.e. through the emission of a $W^{\pm}$ boson. For instance, charm, with electric charge $+2/3$, can change flavor into strange, with electric charge $-1/3$, by emitting a W^+ boson (see *Figure 6.6*).

The D^0 meson contains a charm quark and an anti-up quark, and is the lightest charmed meson with a mass of approximately 1.87 GeV. The D^0 meson can be reconstructed through its hadronic decay $D^0 \rightarrow K^-\pi^+$ (see *Figure 6.7*) with a branching ratio $BR = 3{,}89\%$ [32]. *Figure 6.8* shows the invariant mass distribution of kaons and pions from the run LHC10f7a which shows a pronounced peak around the expected mass of the D^0. One should however be aware of running into D^0s due to the fact that the D^0 meson also could decay through reactions like $D^0 \rightarrow K^-\pi^+\pi^-\pi^+$ [33]. It should however be mentioned that the major source of background radiation however is the combinatorial background of kaons and pions emanating from light flavors. The D^0 cross section from a 7 TeV pp collision compared to FONLL calculations can be seen in *Figure 6.9*, showing a fairly good agreement between the predictions and data.
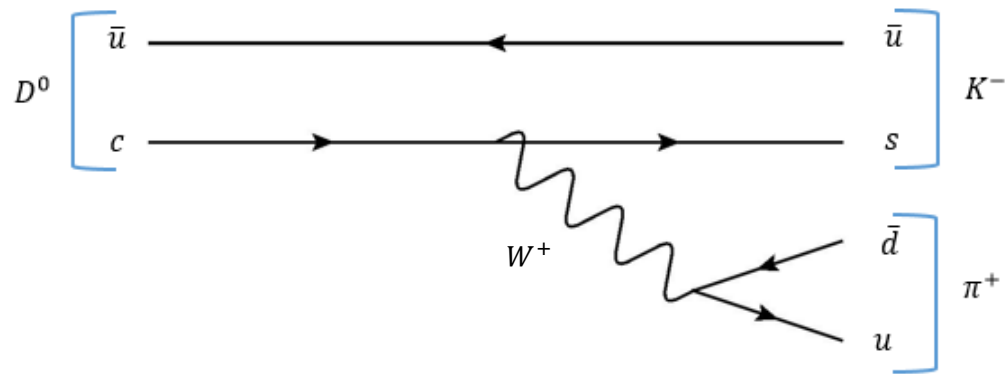
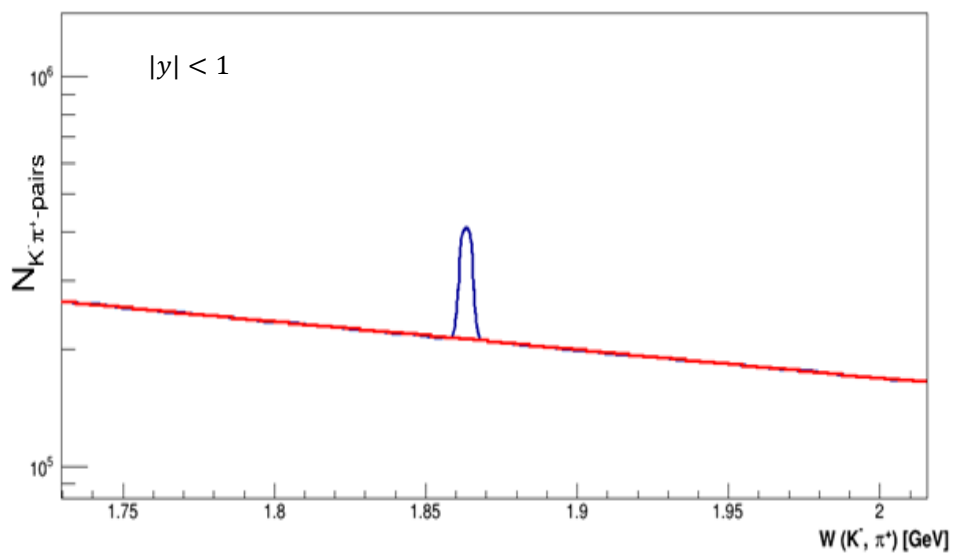Figure 6.7: Feynman diagram depicting the hadronic decay $D^0 \rightarrow K^-\pi^+$.

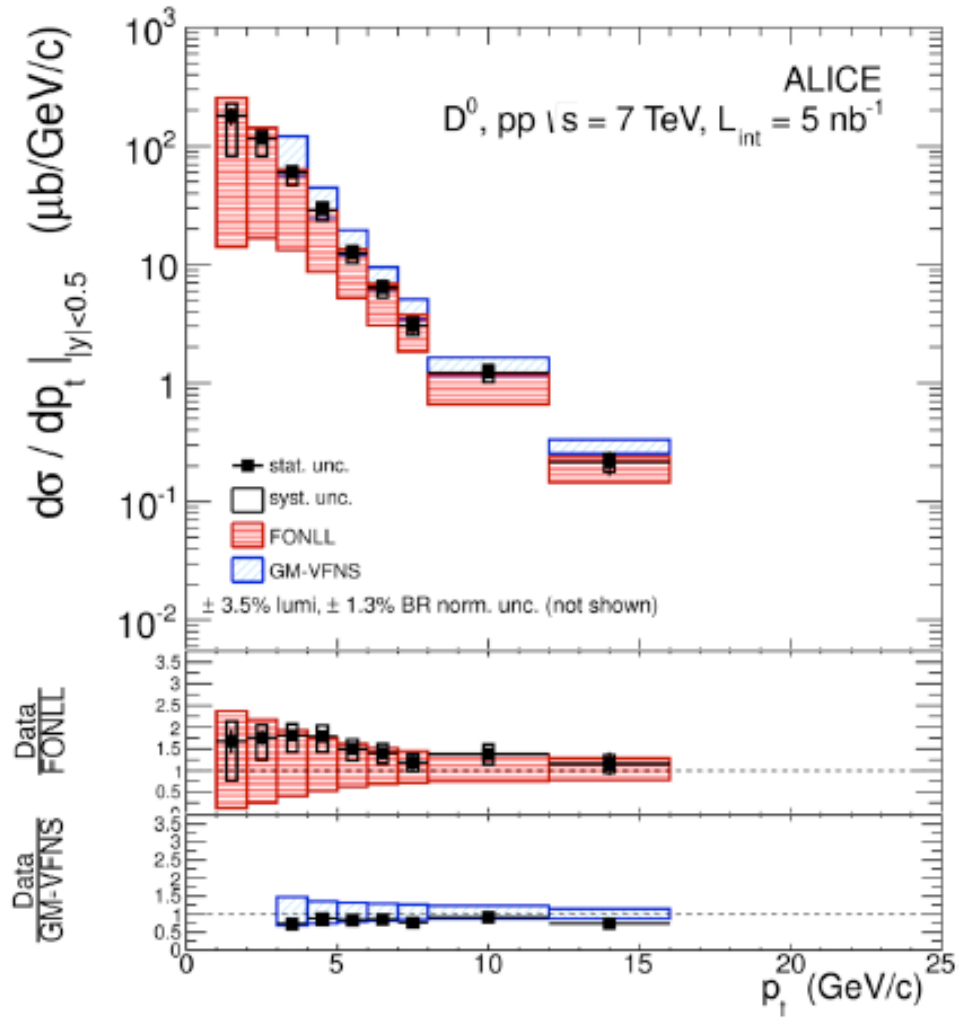Figure 6.8: Invariant mass plot for $K^-\pi^+$ pairs from the enhanced sample.

Figure 6.9: Differential cross section of D^0 from p-p collisions at $\sqrt{s}$ = 7 TeV compared to pQCD predictions [34].

6.3 Heavy Flavor Electron-D^0 Azimuthal Correlations

The angular correlations of D mesons can provide pivotal information on energy loss models of heavy quarks traversing the QGP created in heavy-ion collisions. Studies of light di-hadron angular correlations show that the relative energy loss for light quarks is $\mathcal{O}(10^{-1})$ [35] achieved through comparing pQCD predictions and the I_{AA} as a function of φ. A similar approach for heavy flavors should yield imperative information expounding I_{AA} models. Due to the hard fragmentation of charm, it is reasonable to expect that the D mesons will carry a substantial fraction of the initial heavy flavor momentum. This implies that a study of DD angular correlations should give a good insight into the energy loss of heavy flavors in the QGP. However, experimental constraints such as low reconstruction efficiency requires a somewhat different approach on the study of heavy flavor azimuthal correlations. Another approach is the study of HFE-D^0 azimuthal correlations. In this case, the angular correlations of electrons emerging from heavy flavors and D^0 mesons are of interest. Not only does this imply the ubiquitous of a heavy flavor partonic structure, but also yields the potential of separating charm and beauty contributions since a fraction of D mesons originates from beauty quarks.

The algorithm for the HFE-D^0 analysis can be summarized by (see *App. II* for an excerpt of the actual code)

- Trigger on electrons
- Check if the electron mother is a heavy flavor particle
- Find a D^0
- Calculate the $\Delta\phi = \phi_e - \phi_{D^0}$

All trigger electrons originating from heavy flavor particles, either by means of decaying mesons or a result of the collisions, are known as primary electrons, meaning electrons originating from gamma conversions are not included. However, the D^0 also decays through channels like $D^0 \to K^- e^+ \nu_e$. This causes an enhanced near-side peak since the correlation of the trigger electron and the mother D^0 will have a same-side orientation as seen in *Figure 6.*10. A temporal solution to exclude these "false" trigger electrons is to exclude the D^0 mesons decaying electrons. However, this solution will also exclude the valid trigger case where one correlates an electron originating from a D^0 with a different D^0 meson. To increase the statistics and against any changes in the shape of the distribution, a more appropriate method will be presented. In this method against autocorrelation of the electron and the mother D^0, the macro checks the stack position of the particles and excludes the D^0 if the D^0 is the actual mother of the electron.

Figure 6.11 shows the HFE-D^0 correlations for the enhanced sample and the minimum bias simulation with no p_T cuts. It is apparent that in both the temporal solution, where one excludes all $D^0 \to e$ +anything, and the new solution, where the stack position check is used, the artificially enhanced nearside peak due to the autocorrelation effect is corrected. As expected, the number of entries is increased for the new solution, but the distribution in general is pretty much unchanged. However, there is a clear difference on the near-side when comparing the two sets. The enhanced sample depicts a pronounced
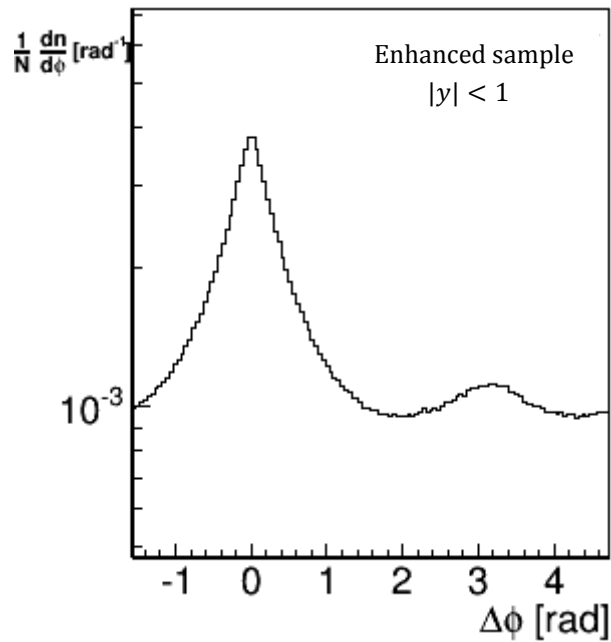
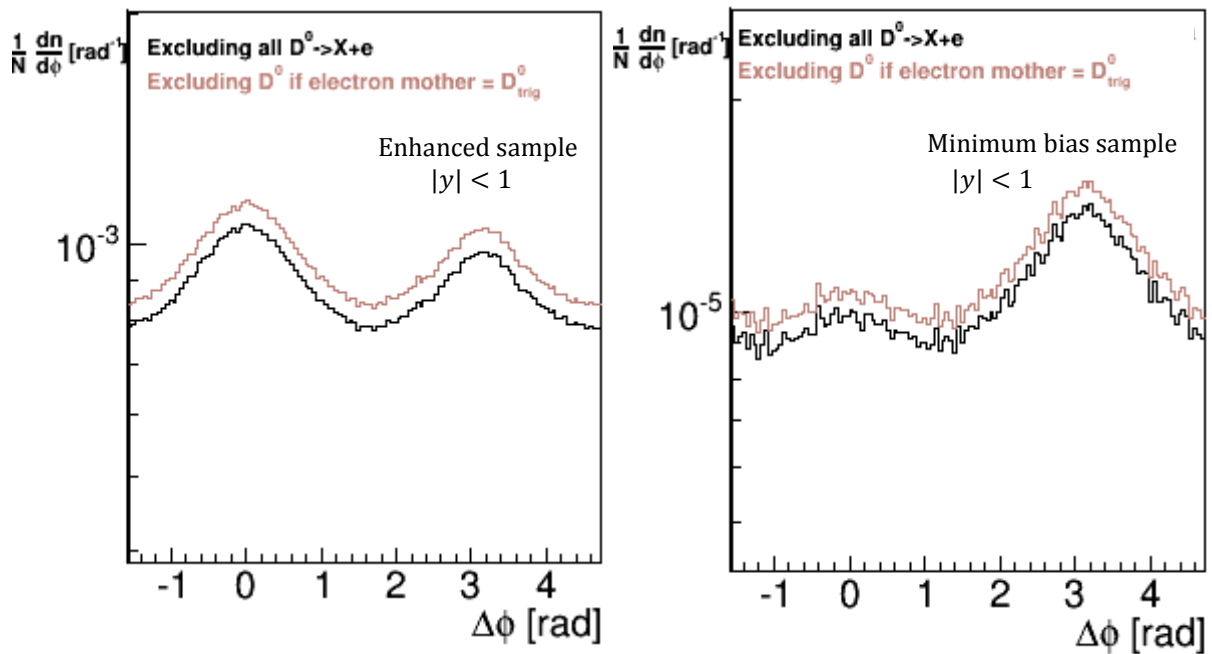*Figure 6.10: HFE-D^0 azimuthal correlations with the autocorrelation in effect from the enhanced sample.*

Figure 6.11: HFE-D^0 azimuthal correlation plot from PYTHIA generated proton-proton collisions at $\sqrt{s}$ = 7 TeV for the runs enhanced sample and the minimum bias set.
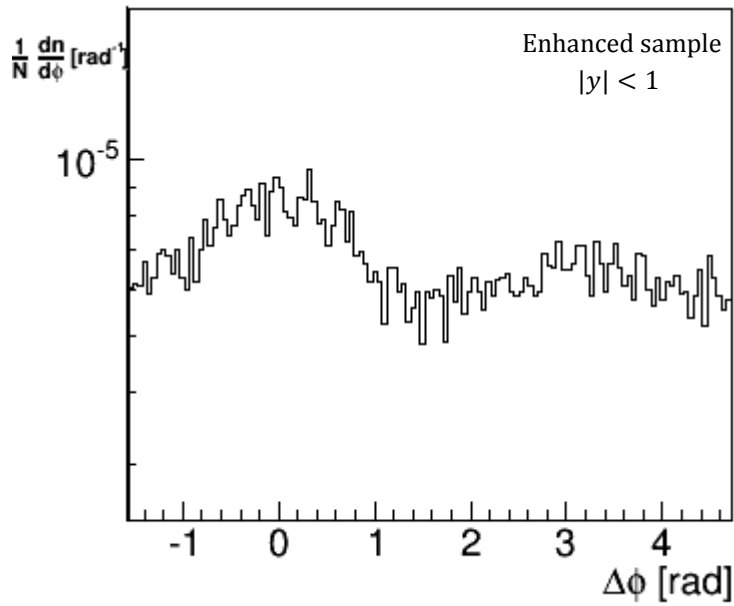
Figure 6.12: HFE-D^0 azimuthal correlation plot from PYTHIA generated proton-proton collisions at $\sqrt{s}$ = 7 TeV for the runs enhanced sample, where the only D^0 mesons correlated with electrons decay according to $D^0 \rightarrow K^-\pi^+$.

peak, whilst the minimum bias set only indicates a small bump. This can be a consequence of the fact that the enhanced sample also is enhanced regarding D meson production ratios along with an intervention of the D^0 decay modes. It should be noted that experimentally, one does not observe this artificial auto-correlation peak on the near-side. This is due to the fact that the electrons are correlated with D^0 mesons which are reconstructed through the decay $D^0 \rightarrow K^-\pi^+$, omitting any chance of auto-correlations. *Figure 6.12* depicts the azimuthal correlations of electrons and D^0 mesons where the decay mode is used as a secondary condition. As seen, the distribution is the same as given in *Figure 6.11*, but with much less statistics.

Adding a momentum cut of $1 \; GeV < D^0_{p_T} < 5 \; GeV$ for the D^0 and an electron p_T cut given by $e_{p_T} > 0.5 \; GeV$, referring to *Figure 6.13*, reveal some interesting properties regarding the correction to the auto-correlation effect. In both the enhanced and the minimum bias sample, there is a perfect overlap on the away side for the auto-correlated distribution and the new stack position distribution. This is to be expected since there shouldn't be any autocorrelation effects on the away-side since a mother and daughter particle predominantly will have a same-side orientation. However, with the introduced momentum cut there appears to be a small change in the azimuthal distributions when comparing the current solution and the new proposal on both the near side and the away side, a feature which is apparent in both data sets. When excluding only the D^0s which are the mother of the trigger electron, there is a suppression in the number of entries compared to the case where one exclude all D^0 decays including the emission of electrons.
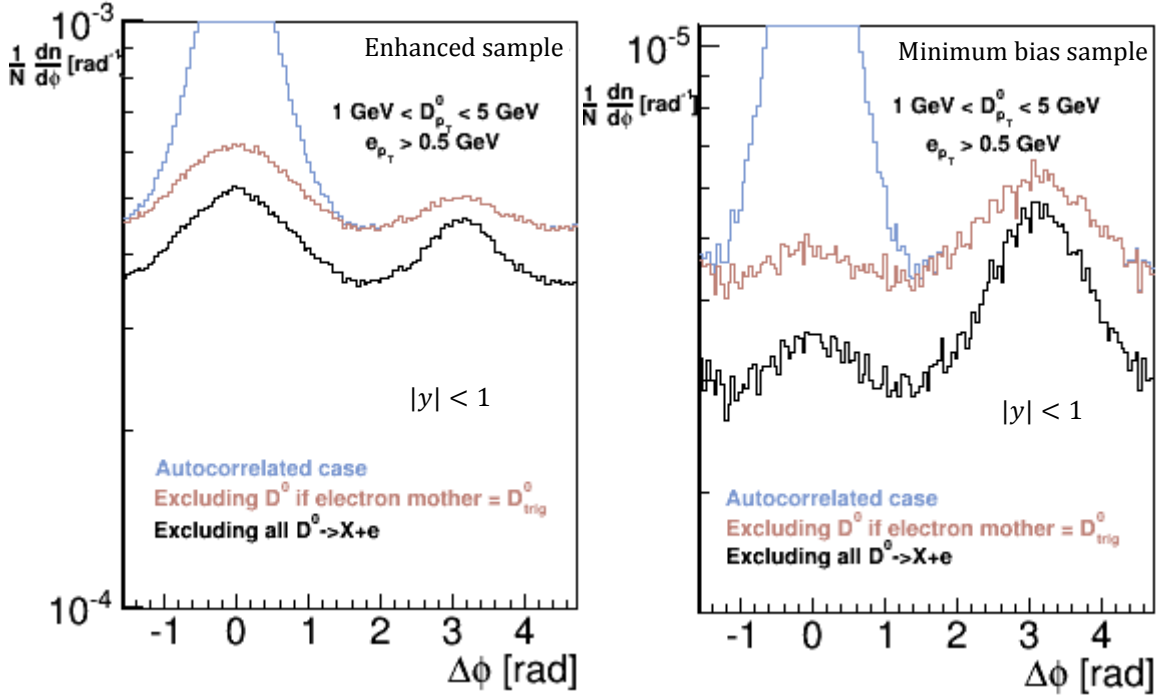
Figure 6.13: HFE-D^0 azimuthal correlation plot from PYTHIA generated pp collisions at $\sqrt{s}$ = 7 TeV for the enhanced and the minimum bias sample, where $1\ GeV < D^0_{p_T} < 5\ GeV$ and $e_{p_T} > 0.5\ GeV$.

Increasing the momentum cut to $5\ GeV < D^0_{p_T} < 10\ GeV$ for the D^0 and $e_{p_T} > 1.5\ GeV$ for the electron further increases the disparity of the two auto-correlation fixes as can be seen in *Figure 6.14*. In this p_T range, the stack position check is a factor of 3 times the current auto-correlation fix on the away side for the minimum bias sample. By adding a very high momentum cut, $D^0_{p_T} > 10\ GeV$ and $e_{p_T} > 1.5\ GeV$, the two distributions representing the auto-correlation fixes are pretty much unchanged when looking at the shape of the distribution, but the number of entries really start to deviate on the away side for both simulation as can be seen in *Figure 6.15*. Not only is there a significant change in the number of statistics, but the shapes of the distributions as well start to deviate. The new approach implies a wider distribution on the away-side, and the ratio between the peaks on the near-side and the away-side decreases.

It is also of great interest to see how the distributions change from quark level, that is, charm and beauty quark $\Delta\phi$ distributions, to the hadronic HFE-D^0 distribution level. Again, since the data sets are PYTHIA generated, the azimuthal correlations of charmed electron-D^0 pairs and beauty electron-D^0 pairs can be investigated in detail. *Figure 6.16* depict the azimuthal correlations of charmed electrons and charmed D^0 mesons compared to the $c\bar{c}$ $\Delta\phi$ distribution for the enhanced sample and the minimum bias sample. It is of interest to note that in the minium bias sample, the charmed electron-charmed D^0 distribution is pretty much constant except for on the away-side, where one can observe a statistically significant deviation. In the enhanced sample on the other hand, one can observe a peak both on the near-side and the away-side.

Figure 6.14: HFE-D^0 azimuthal correlation plot from PYTHIA generated pp collisions at $\sqrt{s}$ = 7 TeV for the enhanced and the minimum bias sample, where $5\ GeV < D^0_{p_T} < 10\ GeV$ and $e_{p_T} > 1.5\ GeV$.

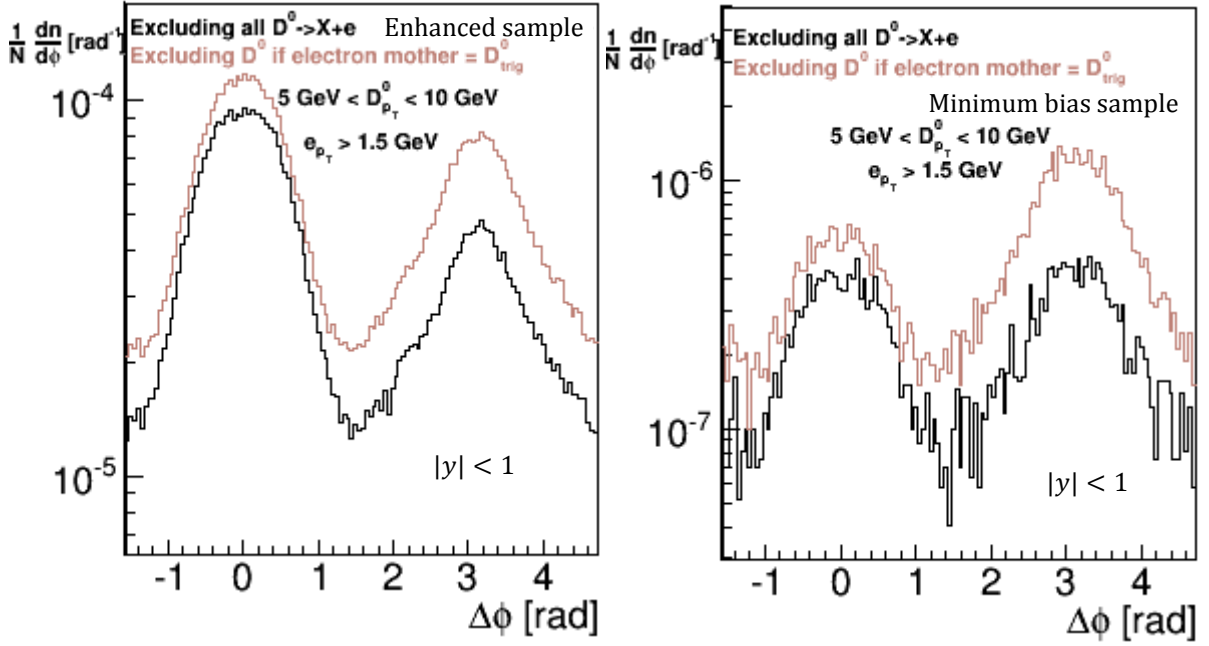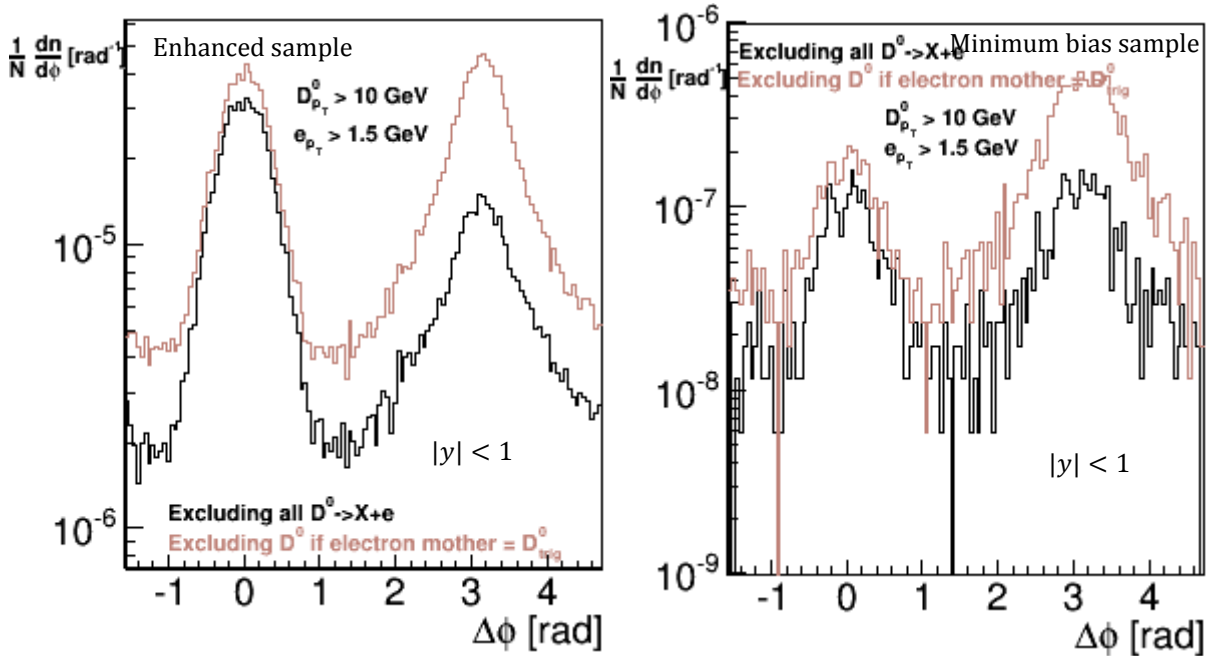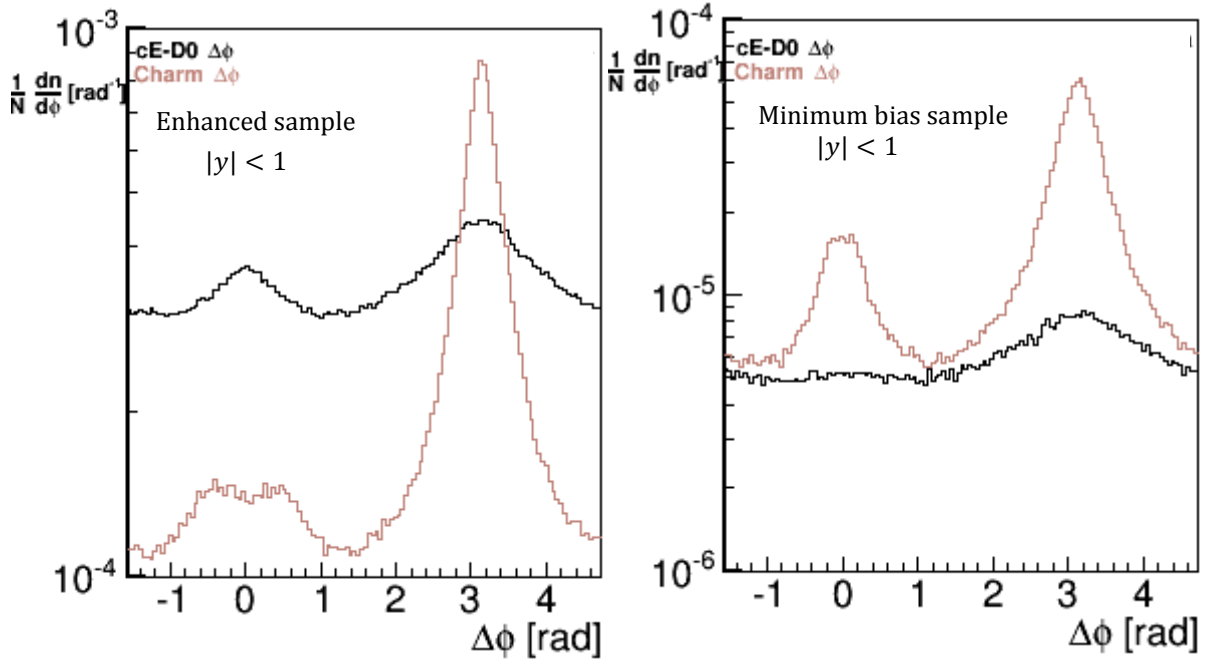*Figure 6.15: HFE-D^0 azimuthal correlation plot from PYTHIA generated pp collisions at $\sqrt{s}$ = 7 TeV for the enhanced and the minimum bias sample, where $D^0_{p_T} > 10\ GeV$ and $e_{p_T} > 1.5\ GeV$.*

Figure 6.16: Charmed electron-D^0 azimuthal correlation plot from PYTHIA generated p-p collisions at $\sqrt{s}$ = 7 TeV for the enhanced and minimum bias sample.
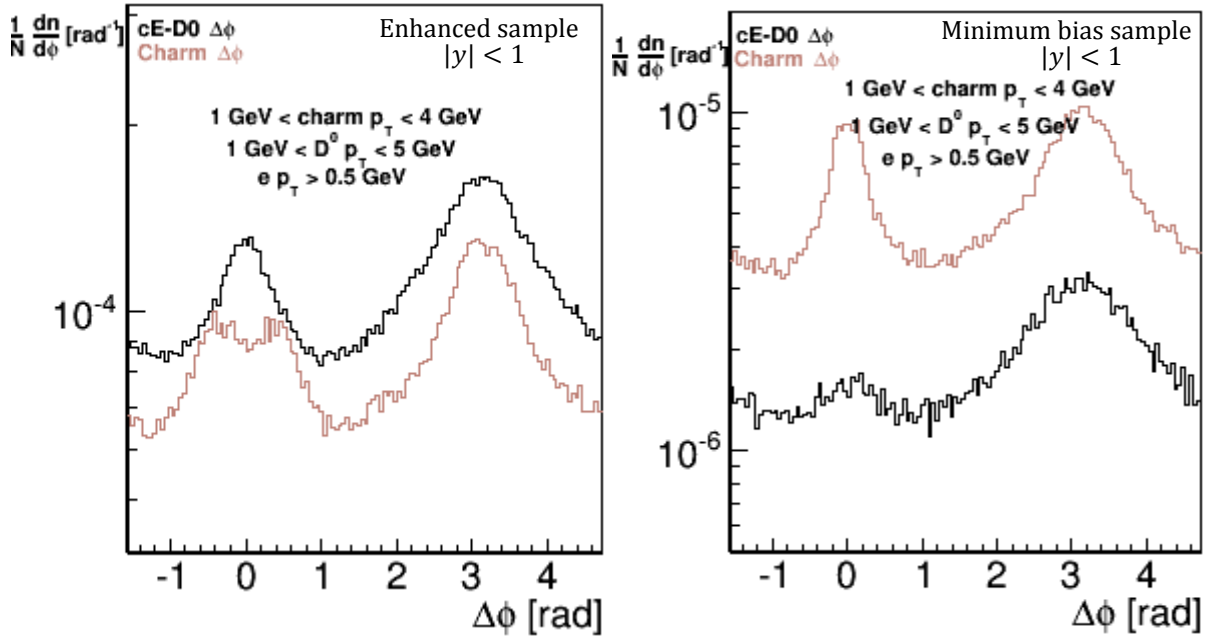

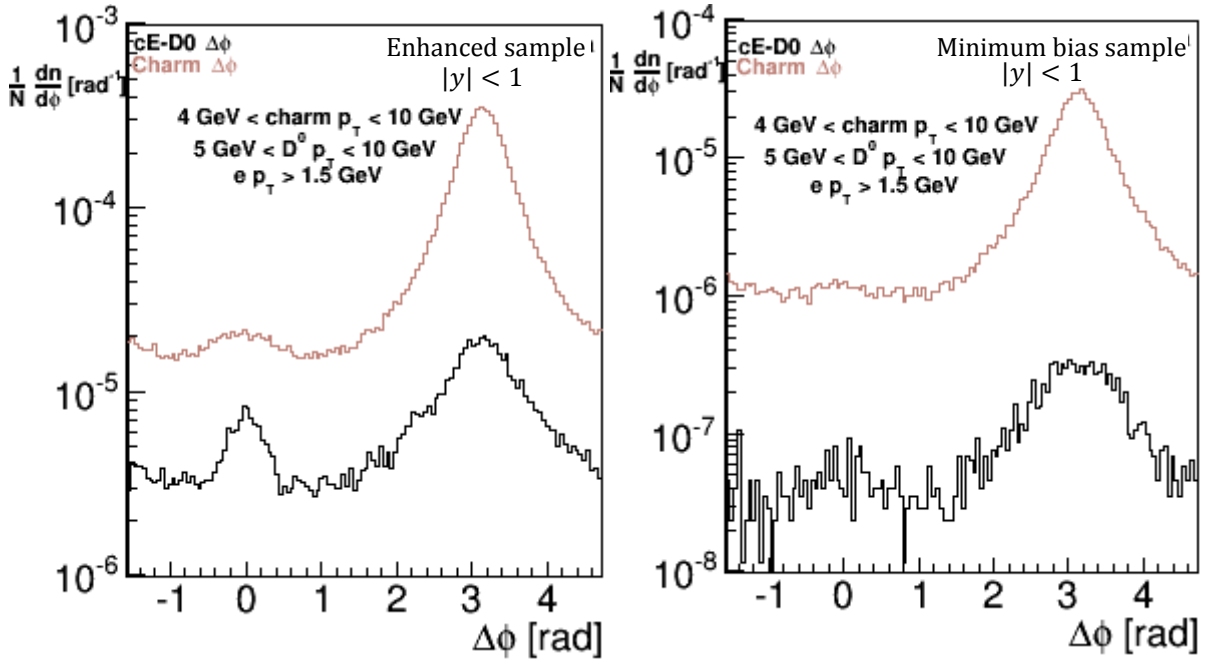*Figure 6.17: Charmed electron-D^0 azimuthal correlation plot from PYTHIA generated pp collisions at $\sqrt{s}$ = 7 TeV for the enhanced and minimum bias sample, where $1\ GeV < D^0_{p_T} < 5\ GeV$, and $e_{p_T} > 0.5\ GeV$ and $1\ GeV < charm_{p_T} < 4\ GeV$.*

Figure 6.18: Charmed electron-D^0 azimuthal correlation plot from PYTHIA generated pp collisions at $\sqrt{s}$ = 7 TeV for the enhanced and the minimum bias sample, where $5\ GeV < D^0_{p_T} < 10\ GeV$, and $e_{p_T} > 1.5\ GeV$ and $4\ GeV < charm_{p_T} < 10\ GeV$.
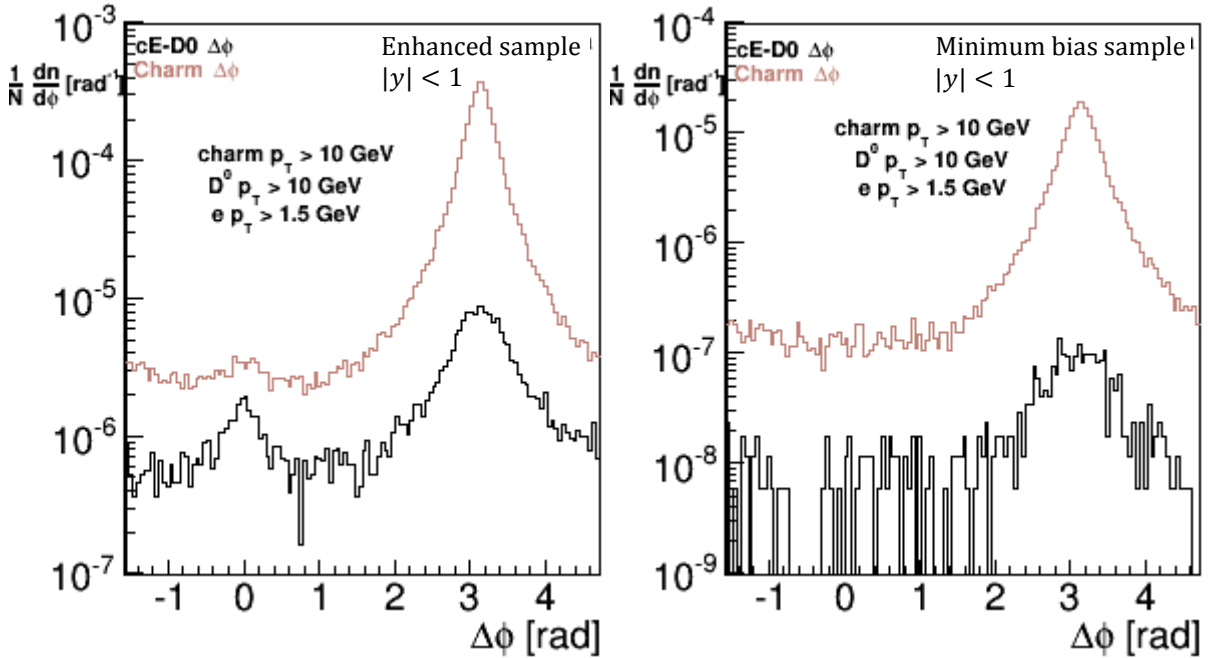

Figure 6.19: Charmed electron-D^0 azimuthal correlation plot from PYTHIA generated pp collisions at $\sqrt{s}$ = 7 TeV for the enhanced and the minimum bias sample, where $D^0_{p_T} > 10\ GeV$, and $e_{p_T} > 1.5\ GeV$ and $charm_{p_T} > 10\ GeV$.
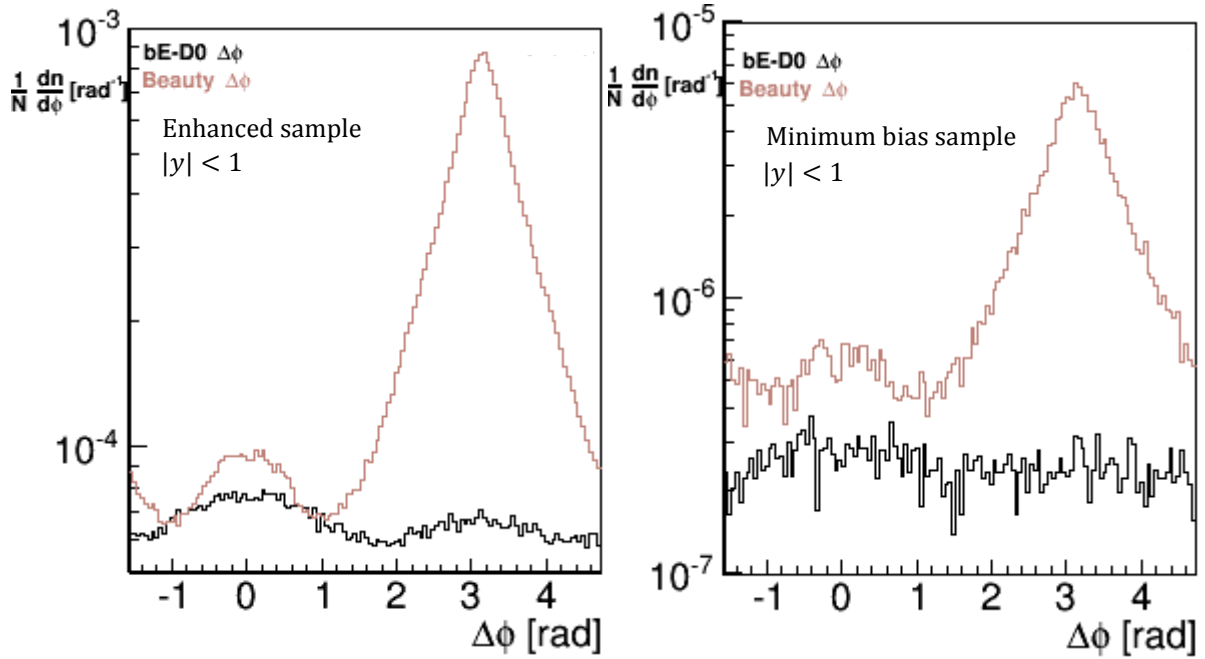
Figure 6.20: Beauty electron-D^0 azimuthal correlation plot from PYTHIA generated pp collisions at $\sqrt{s}$ = 7 TeV for the the enhanced and the minimum bias sample.

Applying a momentum cut given by $1\ GeV < D^0_{p_T} < 5\ GeV$ for the D^0 and $e_{p_T} > 0.5\ GeV$ doesn't really change the charmed electron-D^0 distributions extensively (see *Figure 6.17*), but increasing the cuts further, as given in *Figure 6.18*, corrects the double-peak feature on the near-side. Further increasing the momentum cuts does not drastically change the distributions, as given by *Figure 6.19*. The behaviour of these distributions can also be observed in the beauty electron-beauty D^0 azimuthal correlations given by *Figures 6.20-6.23*, albeit far more subtle. The only main difference is an enhanced peak on the near-side at higher p_T cuts. However, it becomes hard to draw any conclusion on the minimum bias set due to lack of statistics.

Compared to the charm $\Delta\varphi$ distribution, the charmed electron$-D^0$ $\Delta\varphi$ distribution appears to be "smeared", refering again to *Figure 6.16*. This feature is apparent in both samples. As seen, the ratio between the peaks on the away-side and the near-side for the charm $\Delta\varphi$ $\sim\mathcal{O}(10)$, while the charmed electron$-D^0$ $\sim\mathcal{O}(1)$. The width of the charmed electron$-D^0$ $\Delta\varphi$ distribution is also wider, both on the near-side and the away-side. This trend is even more apparent when comparing beauty $\Delta\varphi$ distributions and beauty electron$-$beauty D^0 $\Delta\varphi$ distributions. In both samples, there is a major difference on the away-side, where the peak-to-peak ratio differ by almost an order of magnitude.

Figure 6.21: Beautyd electron-D^0 azimuthal correlation plot from PYTHIA generated pp collisions at $\sqrt{s}$ = 7 TeV for the the enhanced and the minimum bias sample, where $1\ GeV < D^0_{p_T} < 5\ GeV$, and $e_{p_T} > 0.5\ GeV$ and $1\ GeV < beauty_{p_T} < 4\ GeV$.
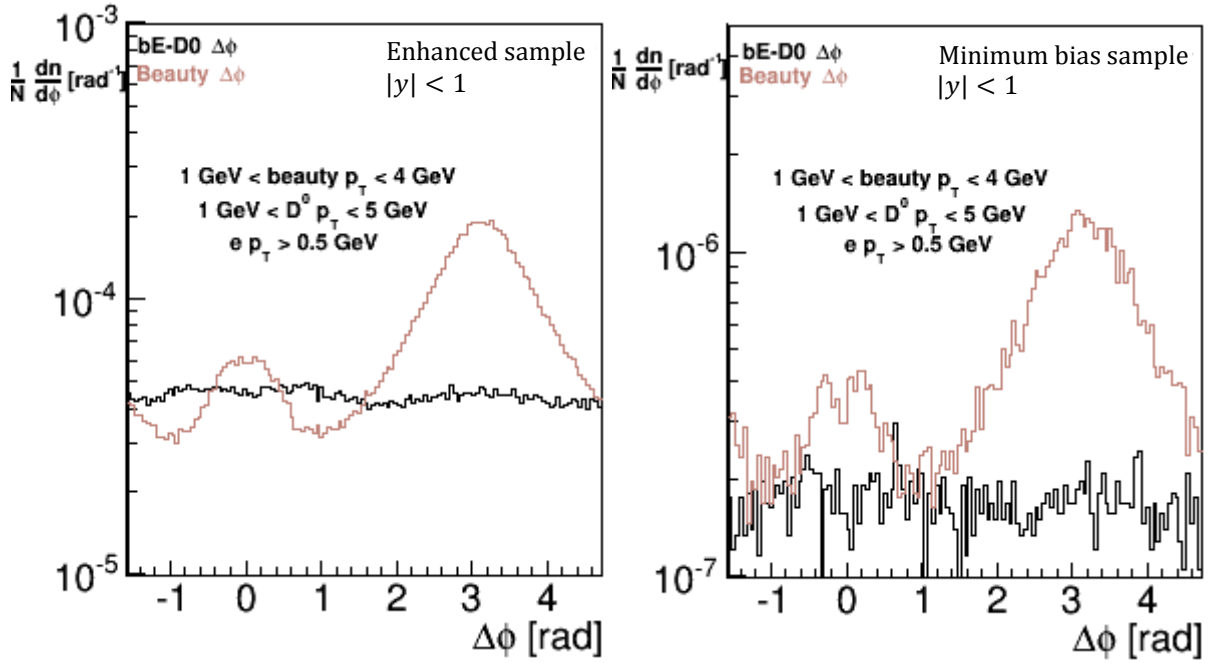

Figure 6.22: Beauty electron-D^0 azimuthal correlation plot from PYTHIA generated pp collisions at $\sqrt{s}$ = 7 TeV for the the enhanced and the minimum bias sample, where $5\ GeV < D^0_{p_T} < 10\ GeV$, and $e_{p_T} > 1.5\ GeV$ and $4\ GeV < beauty_{p_T} < 10\ GeV$.
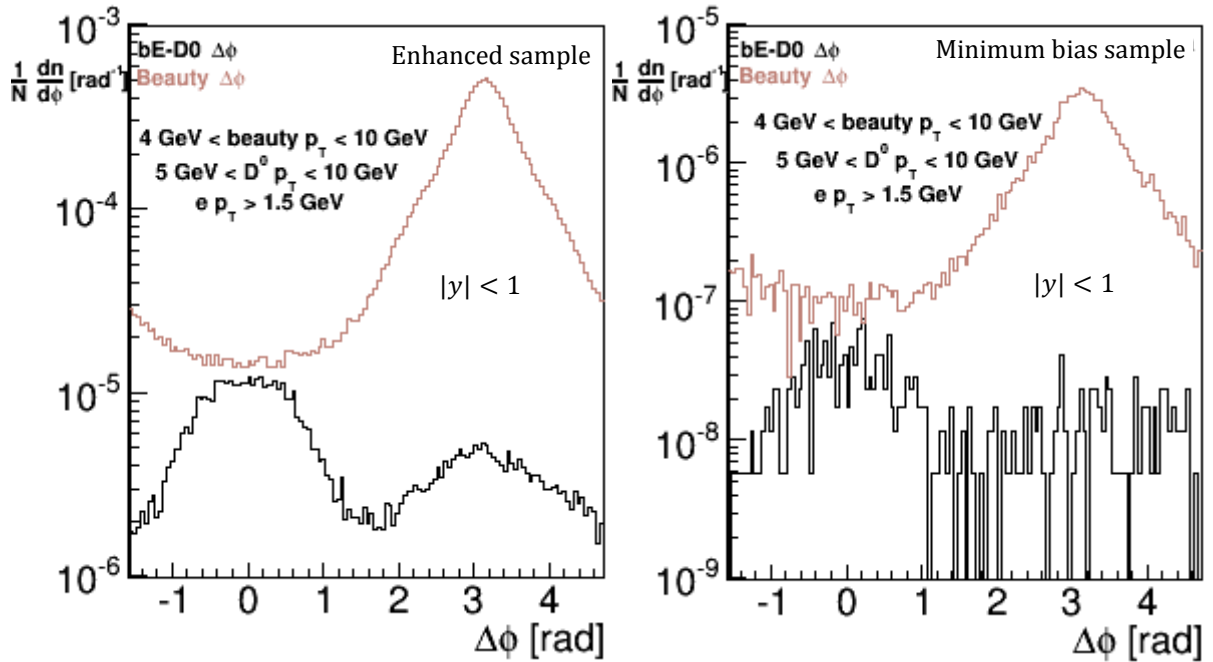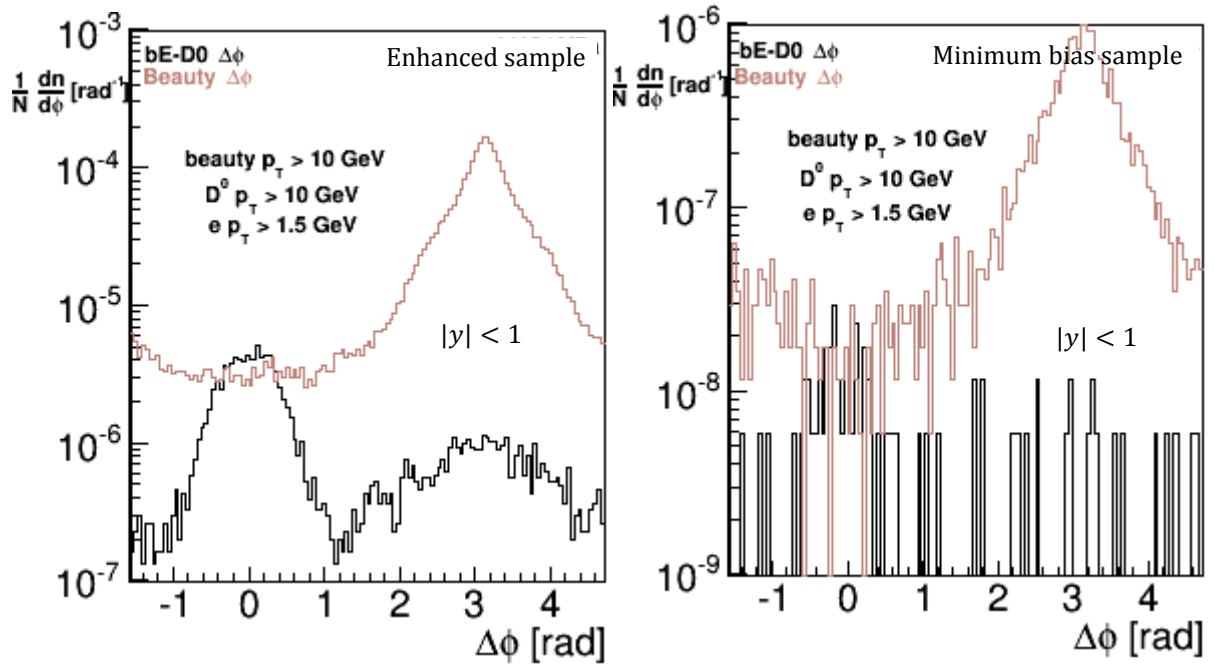
Figure 6.23: Beauty electron-D^0 azimuthal correlation plot from PYTHIA generated pp collisions at $\sqrt{s}$ = 7 TeV for the the enhanced and the minimum bias sample, where $D_{p_T}^0$ > 10 GeV, and e_{p_T} > 1.5 GeV and beauty$_{p_T}$ > 10 GeV.

Chapter 7

Conclusion and Outlook

The main cynosure of this thesis was addressed to the study of the azimuthal correlations of D^0 mesons and heavy flavor electrons from PYTHIA generated proton-proton collisions. The most time consuming part was setting up the analysis software, getting access to GRID, writing the actual analysis code and getting everything to work contemporaneously. A new correction to the auto-correlation effect in HFE-D^0 correlations has been presented with the outcome of both increasing the number of statistics as well as changing the actual distributions.

Two PYTHIA generated Monte Carlo simulations were utilized in this analysis; LHC10f7a and LHC10f6a. The run LHC10f7a is an enhanced sample regarding heavy quarks, while LHC10f6a is a minimum bias run. Although the enhanced sample yields a lot more statistical data, there appear to be some issues with the HFE-D^0 azimuthal correlations compared to the minimum bias sample, especially on the near-side. This feature could be a consequence of the interposing of the decay modes of the D^0 meson. Although the data seem to coincide distribution-wise with the minimum bias run for high p_T cuts, this brings to question the validity of studying azimuthal correlations at low p_T ranges using the enhanced sample, particularly on the near-side.

When comparing the charm $\Delta\varphi$ distributions to the electron$-D^0$ $\Delta\varphi$ plots, the electron$-D^0$ $\Delta\varphi$ distribution seem to keep the orientation of the charm $\Delta\varphi$ plots. At both the partonic scale and the hadronic scale, distributions can be seen both on the near-side, i.e. $\Delta\varphi = 0$, and the away-side, i.e. $\Delta\varphi = \pi$. However, the electron-D^0 $\Delta\varphi$ plots seem to be more "smudged" out. The peak-to-peak ratio when comparing the charm $\Delta\varphi$ distribution to the electron-D^0 $\Delta\varphi$ distribution differs in some cases by almost an order of magnitude, depending on the selected momentum cuts.

The study of other collision systems such as p-p collisions at higher energies, p-Pb collisions or Pb-Pb collisions should yield an even further insight into this matter as the production cross section of the heavy quarks consequently increase, implying a statistical increment. Although there are experimental constraints, it is still of great interest to see if there would be any fundamental changes to the azimuthal correlations according to the simulated data, both on a partonic scale as well as the hadronic. As of today, the ALICE detector is undergoing upgrades, including the improvement of the TPC as well as the TRD which entails better electron selection. The LHC is scheduled to start conduct experiments again in 2015.

Bibliography

[1]   S. Hawking, "On the Shoulders of Giants", First Edition, Penguin Books Ltd, London 2002

[2]   J. Jewett & R. Serway, "Physics for Scientists and engineers with modern physics", Eight Edition, Cengage 2010

[3]   S. Chandra & M. Sharm, "Nuclear and Particle Physics", Alpha Science International Ltd., Oxford, UK, 2012

[4]   E. Gates, "Einstein's Telescope", W.W. Norton & Company, New York 2009

[5]   P. Tipler & R. Llewellyn, "Modern Physics", Fifth Edition, W. H. Freeman and Company, New York 2008

[6]   M. van Leeuwen , "High-pT results from ALICE", arXiv:1201.5205 January 2012

[7]   A.S. Yoon, "Centrality and pT dependence of charged particle RAA in PbPb collisions at psNN = 2.76 ", arXiv:1107.1862v2 2011

[8]   E. Bruna, "D-meson nuclear modication factor and v2 in Pb-Pb collisions at the LHC", arXiv:1401.1698v1 2014

[9]   "The Cern Large Hadron Collider: Accelerator and Experiments", *Volume 1: LHC Machine, ALICE and ATLAS*, Copyright CERN, Geneva 2009, first published electronically as 2008 JINST 3 S08001

[10]   ALICE: https://aliceinfo.cern.ch/Figure/sites/aliceinfo.cern.ch.Figure/ files/Figures/General/jthaeder/2012-Aug-02-ALICE_3D_v0_with_Text.jpg

[11]   Cern-Brochure - 2009 – 003 - Eng

[12]   "The Cern Large Hadron Collider: Accelerator and Experiments", *Volume 1: LHC Machine, ALICE and ATLAS*, Copyright CERN, Geneva 2009, first published electronically as 2008 JINST 3 S08003

[13]   AliRoot: http://aliweb.cern.ch/Offline/ Activities/ Analysis/ AnalysisFramework/ index.html

[14]   The ALICE Offline Bible: http://aliweb.cern.ch/secure/Offline/ sites/ aliweb.cern.ch.Offline/files/uploads/ OfflineBible.pdf

[15]   F.W. Bopp, "RAPIDITY GAPS AND THE Phojet MONTE CARLO", arXiv:hep-ph/9803437v1 1998

[16]   P. Tipler & R. Llewellyn, "Modern Physics", Fifth Edition, W. H. Freeman and Company, New York 2008

[17]   R. Odorico, "Hadronic Production of Charm via Flavor Excitation", *Nuclear Physics B209* 1982

[18]   F. Mandl, & G. Shaw, "Quantum Field Theory", 2nd Edition, School of Physics & Astronomy, The University of Manchester, Manchester, UK, WILEY 2010

[19]   V. Devanathan, "Relativistic Quantum Mechanics and Quantum Field Theory", Alpha Science International LTD., Oxford, UK, 2011

[20]   M. Peskin, "An Introduction to Quantum Field Theory", Westview Press, 1st Edition, 1995

[21]   B. Combridge, "Associated Production of Heavy Flavour States in pp Interactions", *Nuclear Physics B181* 1978

[22]   E. Norrbin & T. Sjöstrand, Production and Hadronization of Heavy Quarks, arXiv:hep-ph/0005110v1 11 May 2000

[23]   M. Cacciari *et al.*, "Charm and Bottom Production in PQCD, Characterization of the Quark Gluon Plasma with Heavy Quarks", Physikzentrum Bad Honnef, June 2008

[24]   R. Nouicer, "Probing Hot and Dense Matter with Charm and Bottom Measurements with PHENIX VTX Tracker", arXiv:1212.3291v1 Dec 2012

[25]   ALICE: https://aliceinfo.cern.ch/Figure/sites/aliceinfo.cern.ch.Figure/files/ Figures/dthomas/2012-Jul-29-CcrossSection.pdf

[26]   T. Sjöstrand *et al.*, "An Introduction to PYTHIA 8.2", arXiv: 1410.3012 Oct 2014

[27]   PYTHIA: http://home.thep.lu.se/~torbjorn/Pythia.html

[28]   T. Sjöstrand *et al.*, "PYTHIA 6.2 Physics and Manual", arXiv:hep-ph/0603175v2 12 May 2006

[29]   A. Mischke, "Heavy-flavor correlation measurements via electron azimuthal correlations with open charm mesons", arXiv:0710.2599v1 Oct 2007

[30]   A. Mischke, "Heavy-flavor particle correlations in STAR via electron azimuthal correlations with *D*0 mesons", *J. Phys. G: Nucl. Part. Phys. 35* 2008

[31] X. Zhu, "DD correlations as a sensitive probe for thermalization in high energy nuclear collisions", *Physics Letters B 647* 2007

[32] Particle Data Group: http://pdg.lbl.gov

[33] A. Geromitsos, "Non Photonic e−D0 correlations in p+p and Au+Au collisions at psNN = 200 GeV", arXiv:0911.2490v1 2009

[34] R. Grajcarek, "Measurement of heavy- avor production in PbPb collisions at the LHC with ALICE", arXiv:1209.1925v1 2012

[35] T. Renk, "Using Hard Dihadron Correlations to constrain Elastic Energy Loss", arXiv:1110.2313v1 2011